Available online at www.sciencedirect.com
ScienceDirect
Journal of Sound and Vibration 315 (2008) 509–535
JOURNAL OF SOUND AND VIBRATION
www.elsevier.com/locate/jsvi

Local and global vibration of thin-walled members subjected to compression and non-uniform bending

R. Bebiano, N. Silvestre, D. Camotim*

Department of Civil Engineering and Architecture, ICIST/IST, Technical University of Lisbon, Av. Rovisco Pais, 1049-001 Lisboa, Portugal

Received 13 February 2008; received in revised form 20 February 2008; accepted 20 February 2008
The peer review of this article was organised by the Guest Editor
Available online 9 April 2008

Abstract

The local-plate, distortional and global vibration behaviour of thin-walled steel channel members subjected to compression and/or non-uniform bending is studied. This investigation is carried out by means of a very recently developed Generalised Beam Theory (GBT) formulation, which takes into account the geometrically nonlinear stiffness reduction caused by the presence of (i) longitudinal stress gradients and (ii) the ensuing shear stresses. Taking advantage of the GBT modal features, one analyses the effect of the applied load and bending moment gradient on the small amplitude vibration behaviour of the loaded members (beam-columns). For validation purposes, some GBT-based results are compared with values yielded by either shell finite element analyses, performed in commercial codes, or experimental results available in the literature.

1. Introduction

In order to properly assess the dynamic behaviour of thin-walled steel members, one must acquire in-depth knowledge concerning both its local (local-plate or distortional) and global vibration behaviours, i.e., identify all the relevant vibration modes and evaluate the associated natural frequencies. Moreover, since in several applications steel members are subjected to *simultaneous* static and dynamic actions (e.g., the effects of heavy machinery or seismic activity), designers are faced with the need to assess their dynamic response—in order to perform this task, they must be equipped with efficient analytical and/or numerical tools to analyse the vibration behaviour of members acted upon by more or less significant internal forces and/or moments.

Up to now, a fairly large amount of research work has been devoted to the study of the influence of *local deformations* on the vibration behaviour of *load-free* members (e.g., Refs. [1–4]). However, the same cannot be said about *loaded* members, even though the *global* vibration behaviour of columns and beams has been the subject of several studies (e.g., Refs. [5–8])—concerning beams, it is worth mentioning (i) the closed-form

*Corresponding author. Fax: +351 21 8497650.
E-mail address: dcamotim@civil.ist.utl.pt (D. Camotim).

0022-460X/$ - see front matter © 2008 Elsevier Ltd. All rights reserved.
doi:10.1016/j.jsv.2008.02.036

Nomenclature

A cross-section area
B_{ik}, C_{ik}, D_{ik} GBT basic (linear) stiffness tensorial components
b, h wall width and thickness
$\mathbf{d}^e$ finite element displacement vector
$\mathbf{d}$ global displacement vector
E, G, v Young's modulus, shear modulus and Poisson's ratio
I_3 minor axis moment of inertia
$\mathbf{K}^e$, $\mathbf{G}^e$, $\mathbf{M}^e$ finite element stiffness, geometric and inertia matrices
$\mathbf{K}$, $\mathbf{G}$, $\mathbf{M}$ global stiffness, geometric and inertia matrices
L member length
M, N applied bending moment and axial compression
n number of cross-section walls
n_d number of GBT deformation modes considered
n_s number of longitudinal half-waves
P_k GBT modal participation factor
Q_{ik}, R_{ik} GBT out-of-plane and in-plane inertia tensorial components
S cross-section overall width
$S_j(s)$ first moment of area
X^{σ}_{jik}, X^{τ}_{jik} GBT geometric stiffness tensorial components related to longitudinal and shear stresses
$u_k(s)$, $v_k(s)$, $w_k(s)$ modal warping, transverse membrane and flexural displacement functions
u, v, w displacement field components
U, T member strain and kinetic energies
W^0_j GBT generalised normal stress resultant
x, s, z wall (plate) coordinate axes
X, Y, Z member global coordinate axes
$Y(t)$ time-dependent amplitude function
α applied load level (fraction of critical value)
$\phi_k(x)$, $\zeta_k(x,t)$ longitudinal modal amplitude functions
λ load parameter
Π^{σ}, Π^{τ} potentials of the applied longitudinal and shear stresses
ρ member mass density
σ_{ij}, ε_{ij}, γ_{ij} stress, strain and membrane shear strain components
ω angular frequency
ω_{α} angular frequency of member loaded at level α
$\psi_i(\xi = x/L_e)$ Hermite cubic polynomials
$(.)_{,X}$ derivative with respect to X
$(^F)$, $(^M)$ flexural and membrane components
$(^L)$, $(^{NL})$ linear and nonlinear components

analytical solutions for the flexural–torsional vibration under uniform or variable bending moments, developed by Joshi and Suryanarayan [6,7], and (ii) the analytical solution of the flexural vibration of long simply supported beams subjected to their own weight, reported by Shih et al. [8]. Indeed, few papers deal with the local vibration of loaded thin-walled members and practically all of them concern columns—e.g., the investigations undertaken by Ogha et al. [9] and Okamura and Fukasawa [10].

Until recently, the local and/or global vibration analysis of thin-walled members could only be performed by resorting to either shell finite element analysis (SFEA) [11] or analyses based on the semi-analytical finite strip method (FSM) [12]. Generalised Beam Theory (GBT), originally proposed by Schardt [13] and extensively developed at the Technical University of Lisbon in the last few years (e.g., Refs. [14–16]), incorporates both local and global cross-section deformations. Concerning vibration analysis, the first GBT formulation was developed by Schardt and Heinz [17], who employed it to analyse the *local* and *global* vibration behaviour of load-free isotropic thin-walled members. Later, Silvestre [18] and Silvestre and Camotim [19–21] extended this formulation to cover (i) load-free FRP composite orthotropic members, (ii) cold-formed steel-compressed members and (iii) FRP composite orthotropic members under compression or major axis bending—moreover, a study dealing with the influence of pure bending in steel I-section beams was reported in Ref. [14]. However, all these works deal exclusively with members acted upon by *uniform* axial force and bending moment diagrams.

The objective of this paper is to present the development and illustrate the application of a novel GBT formulation to analyse the vibration behaviour of thin-walled members acted upon by loadings that may include combinations of axial force and uniform or non-uniform bending (as well as the ensuing shear

stresses).[1] The formulation involves the numerical implementation of a GBT-based beam finite element (the main steps are presented here) and is employed to study the local and global vibration behaviour of (i) simply supported lipped channel beams acted upon by *uniformly distributed transverse loads* and (ii) plain channel cantilevers subjected to axial and transverse *tip point loads*, both cases involving non-uniform bending and shear—the investigation focuses mainly on the combined effect of the applied load level and bending moment gradients.

One takes advantage of the unique modal properties of GBT, which (i) make it possible to perform accurate analyses involving only a few degrees of freedom and (ii) provide vibration mode representations expressed as linear combinations of deformation modes with clear structural meanings. Finally, for validation purposes, the GBT-based results are compared with the values obtained experimentally by other authors and/or yielded by FEA carried out in the commercial codes ANSYS or ABAQUS.

2. GBT formulation

Since the cross-section displacement field is expressed as a linear combination of structurally meaningful deformation modes, the GBT analyses (i) lead to equilibrium equations written in a rather convenient form and (ii) enable the performance of "doubly modal" analyses that provide an in-depth and fresh insight on the mechanics of the vibration behaviour of prismatic thin-walled members. In order to derive the GBT equilibrium equations, consider the prismatic thin-walled member depicted in Fig. 1(a), which has a supposedly arbitrary (*n*-walled) open cross-section—also shown is the member global coordinate system *X*–*Y*–*Z* (longitudinal, major and minor axis). Moreover, local coordinate systems *x*–*s*–*z* are adopted in each wall, as shown in Fig. 1(b), where *x* (parallel to *X*) and *s* define the wall mid-plane, and *z* is measured along the thickness *h*—when expressed in this coordinate system, the mid-line displacement field components are designated as *u*, *v* and *w*. According to the classical thin-walled beam theory [22], the displacement components are expressed as

$$u(x,s,t)=u_k(s)\zeta_{k,x}(x,t),\quad v(x,s,t)=v_k(s)\zeta_k(x,t),\quad w(x,s,t)=w_k(s)\zeta_k(x,t) \tag{1}$$

where (i) $(\cdot)_{,x}=\partial(\cdot)/\partial x$, (ii) $u_k(s)$, $v_k(s)$ and $w_k(s)$ are the cross-section deformation mode components and (iii) $\zeta_k(x,t)$ are the amplitude functions describing their variation both along the longitudinal direction and with time *t*. In vibration analysis of thin-walled members, one commonly assumes null mid-surface membrane shear strains ($\gamma_{xs}^{M.L}=0$—"Vlasov's hypothesis") and transverse extensions ($\varepsilon_{ss}^{M}=0$), as well as the classical Kirchhoff–Love hypotheses. Then, the relevant non-null strain components are

$$\varepsilon_{xx}^{M.L}=u_{,x},\quad \varepsilon_{xx}^{M.NL}=(v_{,x}^2+w_{,x}^2)/2,\quad \varepsilon_{xx}^{F}=-zw_{,xx} \tag{2}$$

$$\gamma_{xs}^{F}=-2zw_{,xs},\quad \gamma_{xs}^{M.NL}=w_{,s}w_{,x},\quad \varepsilon_{ss}^{F}=-zw_{,ss} \tag{3}$$

where superscripts $(^M)$ and $(^F)$ identify membrane and flexural components, and the former include linear $(^L)$ and nonlinear $(^{NL})$ terms. The nonlinear terms in Eqs. (2)–(3) are essential to obtain the geometric stiffness matrices related to the applied loading—in particular, the nonlinear membrane shear strain plays a crucial role in the presence of non-uniform applied bending moments. After incorporating Eq. (1) into Eqs. (2) and (3), one obtains the variations of the above strain components, given by

$$\delta\varepsilon_{xx}^{M.L}=u_k\delta\zeta_{k,xx},\quad \delta\varepsilon_{xx}^{M.NL}=(v_iv_k+w_iw_k)\zeta_{i,x}\delta\zeta_{k,x},\quad \delta\varepsilon_{xx}^{F}=-zw_k\delta\zeta_{k,xx} \tag{4}$$

$$\delta\gamma_{xs}^{F}=-2zw_{k,s}\delta\zeta_{k,x},\quad \delta\gamma_{xs}^{M.NL}=w_{i,s}w_k(\zeta_i\delta\zeta_{k,x}+\zeta_{k,x}\delta\zeta_i),\quad \delta\varepsilon_{ss}^{F}=-zw_{k,ss}\delta\zeta_k \tag{5}$$

[1] At this stage, it should be made clear that this work deals exclusively with *small amplitude* (linear) vibrations and that all the geometrically nonlinear effects stem from the presence of applied loads causing compression and (non-uniform) bending. Indeed, in the problems handled by the GBT formulation developed in this paper, the variation of the natural frequencies and vibration mode shapes stems solely from the applied loads. Phenomena similar to the "hardening" and "softening" ones might occur in thin-walled members vibrating under applied loads with varying magnitudes—a load increase (decrease) causes a stiffness drop (raise) that "softens" ("hardens") the member (small amplitude) vibration behaviour.

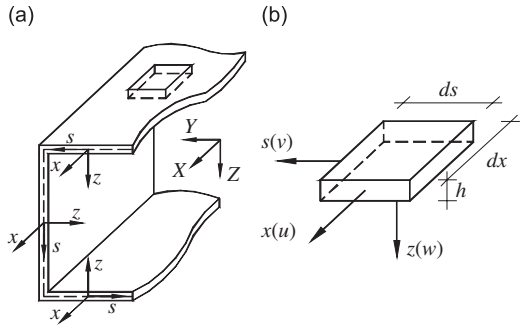

Fig. 1. (a) Arbitrary prismatic open-section thin-walled member and global coordinate system and (b) infinitesimal wall element with its local coordinate system and displacement components.

2.1. Hamilton's principle

In order to perform vibration analyses of thin-walled members acted by static loads, the application of Hamilton's principle, leading to the member dynamic equilibrium equations, reads

$$\int_{t_1}^{t_2} \delta(U + \Pi - \mathrm{T})\,\mathrm{d}t = 0 \tag{6}$$

where U and T are the member total strain and kinetic energies and Π is the potential of the applied loads. Their first variations are given by (L, S and h are the member length, cross-section mid-line overall width and wall thickness)

$$\delta U = \int_L \int_S \int_h \left(\sigma_{xx}^M \delta\varepsilon_{xx}^M + \sigma_{xx}^F \delta\varepsilon_{xx}^F + \sigma_{ss}^F \delta\varepsilon_{ss}^F + \tau_{xs}^F \delta\gamma_{xs}^F\right) \mathrm{d}z\,\mathrm{d}s\,\mathrm{d}x \tag{7}$$

$$\delta T = \int_L \int_S \int_h \left(\rho u_{,t}^P \delta u_{,t}^P + \rho v_{,t}^P \delta v_{,t}^P + \rho w_{,t}^P \delta w_{,t}^P\right) \mathrm{d}z\,\mathrm{d}s\,\mathrm{d}x \tag{8}$$

$$\delta\Pi = \delta\Pi_\sigma + \delta\Pi_\tau = \int_L \int_S \int_h \left(\sigma_{xx}^0 \delta\varepsilon_{xx}^{M.NL} + \tau_{xs}^0 \gamma_{xs}^{M.NL}\right) \mathrm{d}z\,\mathrm{d}s\,\mathrm{d}x \tag{9}$$

where ρ is the material mass density, σ_{xx}^0 and τ_{xs}^0 are the applied longitudinal normal and shear stress fields and u^P, v^P and w^P are the displacement components of an arbitrary wall point P, related to their mid-line ($z = 0$) counterparts u, v and w by means of

$$u^P = u - z w_{,x}, \quad v^P = v - z w_{,s}, \quad w^P = w \tag{10}$$

The stress components appearing in Eq. (7), each of them multiplying the corresponding strain component, are obtained from the plane stress constitutive relations (note that, in order to comply with the classical beam theories, one assumes that no Poisson's effects are included in the membrane longitudinal stresses σ_{xx}^M):

$$\begin{Bmatrix} \sigma_{xx}^F \\ \sigma_{ss}^F \\ \tau_{xs}^F \end{Bmatrix} = \frac{E}{1-v^2} \begin{bmatrix} 1 & v & 0 \\ v & 1 & 0 \\ 0 & 0 & (1+v)/2 \end{bmatrix} \begin{Bmatrix} \varepsilon_{xx}^F \\ \varepsilon_{ss}^F \\ \gamma_{xs}^F \end{Bmatrix} \quad \sigma_{xx}^{M.L} = E\varepsilon_{xx}^{M.L} \tag{11}$$

where E and v are the material Young's modulus and Poisson's ratio. After incorporating the appropriate terms of Eqs. (4)–(5) and relation (11) into (7), one obtains

$$\delta U = \int_L (C_{ik}\zeta_{k,xx}\delta\zeta_{i,xx} + D_{ik}\zeta_{k,x}\delta\zeta_{i,x} + B_{ik}\zeta_k\delta\zeta_i)\,\mathrm{d}x \tag{12}$$

where C_{ik}, D_{ik} and B_{ik} are second-order tensors describing the member linear stiffness behaviour. In members with uniform wall thickness ($h(s)\equiv h$) and material stiffness ($E(s)\equiv E$) (the only ones dealt with in this work),

their components read

$$C_{ik} = E\int_S \left[hu_iu_k + \frac{h^3}{12(1-\nu^2)}w_iw_k\right]\mathrm{d}s \quad B_{ik} = \frac{Eh^3}{12(1-\nu^2)}\int_S w_{i,ss}w_{k,ss}\,\mathrm{d}s$$
$$D_{ik} = \frac{Gh^3}{3}\int_S \left[w_{i,s}w_{k,s} - \frac{\nu}{2(1-\nu)}(w_iw_{k,ss} + w_kw_{i,ss})\right]\mathrm{d}s \tag{13}$$

where G is the material shear modulus, which can be expressed as a function of E and ν. It is worth noting that matrices C_{ik}, D_{ik} and B_{ik} concern *generalised warping* (primary and secondary), *generalised torsion* and *wall transverse bending*. Incorporating Eq. (10) into (8), the first variation of the member kinetic energy reads

$$\delta T = \int_L (Q_{ik}\zeta_{k,xt}\delta\zeta_{i,xt} + R_{ik}\zeta_{k,t}\delta\zeta_{i,t})\mathrm{d}x \tag{14}$$

where, for a uniform mass density ($\rho(s)\equiv\rho$), the second-order tensors Q_{ik} and R_{ik} are given by

$$Q_{ik} = \rho h\int_S u_iu_k\,\mathrm{d}s + \frac{\rho h^3}{12}\int_S w_iw_k\,\mathrm{d}s$$
$$R_{ik} = \rho h\int_S (v_iv_k + w_iw_k)\,\mathrm{d}s + \frac{\rho h^3}{12}\int_S w_{i,s}w_{k,s}\,\mathrm{d}s \tag{15}$$

They concern the influence of the inertia forces associated with *out-of-plane* and *in-plane* cross-section displacements—in both cases, the first and second terms correspond to translational and rotational inertia forces.

As for the geometrically nonlinear effect associated with the applied loads, let us consider a member subjected to a longitudinal stress field given by

$$\sigma^0_{xx} = Eu_j\zeta^0_{j,xx} \tag{16}$$

where $u_j\zeta^0_{j,xx}$ ($j = 1, \ldots, 4$) are the mid-line axial displacements—note that the flexural components of the applied longitudinal stresses are neglected. After incorporating Eqs. (4b) and (16) into (9a), one obtains the expression for the virtual work done by σ^0_{xx},

$$\delta\Pi_\sigma = \int_L W^0_j X^\sigma_{jik}\zeta_{k,x}\,\delta\zeta_{i,x}\,\mathrm{d}x$$
$$W^0_j = C_{jj}\zeta^0_{j,xx} \tag{17}$$

where (i) W^0_j is a vector whose components are normal stress resultants due to the applied loads, namely W^0_1 (axial force), W^0_2 (major axis bending moment), W^0_3 (minor axis bending moment) and W^0_4 (bimoment), each associated with a displacement field $u_j\zeta^0_{j,xx}$ and (ii) X^σ_{jik} are the associated geometric stiffness matrices, given by

$$X^\sigma_{jik} = \frac{Eh}{C_{jj}}\int_S u_j(v_iv_k + w_iw_k)\,\mathrm{d}s \tag{18}$$

Next, one addresses the virtual work done by the applied shear stresses τ^0_{xs}, due to the non-uniform applied bending moments, which deserves special attention. Since Vlasov's null *linear* shear strain hypothesis ($\gamma^{M.L}_{xs} = 0$) is adopted, τ^0_{xs} must be evaluated from longitudinal stress equilibrium (instead of a constitutive relation—a well-known inconsistency of the thin-walled beam theories): the longitudinal stress gradients must be balanced by means of shear stress distributions.[2]

2.1.1. Applied (pre-buckling) shear stress distribution

To illustrate the determination of the shear stress distribution, consider, without any loss of generality, the plain channel beam shown in Fig. 2(a), together with its *global* coordinate system X– Y–Z. As for Fig. 2(b), it

[2]In this work, only the shear stresses due to bending moment longitudinal gradients are dealt with. A similar approach could be adopted to also account for shear stresses caused by longitudinally varying bimoments (required to balance the warping normal stresses caused by non-uniform torsion).

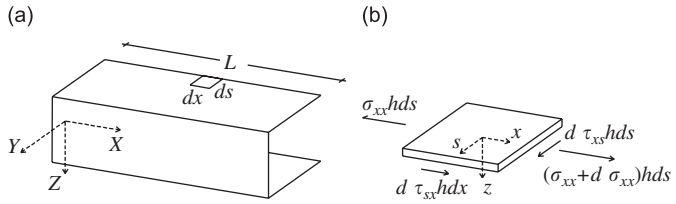

Fig. 2. (a) Beam and global coordinates and (b) wall element with the acting stress resultants.

depicts an infinitesimal wall element located at the beam upper flange end (see Fig. 2(a)), its *local* coordinate system x–s–z and the resultants of the (positive) acting longitudinal normal and shear stresses. By imposing equilibrium along the $x \equiv X$-axis, which involves the acting longitudinal normal stresses and shear stresses (see Fig. 2(b)), and taking into account Eqs. (16) and (17b), one obtains

$$\mathrm{d}\tau^0_{xs} = -\frac{EW^0_{j,x}}{C_{jj}} u_j \,\mathrm{d}s \tag{19}$$

where $W^0_{j,x}$ is the acting shear force (recall that W^0_j is a bending moment—$j = 2$ or 3). The value of the shear stress acting at a given point, $\tau^0_{xs}(x,s)$, is evaluated by integrating Eq. (19) along the mid-line width comprised between a chosen section end and that point [23]—one then obtains

$$\tau^0_{xs}(x,s) = -\frac{EW^0_{j,x} S_j(s)}{C_{jj} h} \tag{20}$$

where $S_j(s)$ is the first moment of that same area, with respect to Y ($j = 2$) or Z ($j = 3$)—see Fig. 2(a). By incorporating Eqs. (5b) and (20) into (9b), one obtains

$$\delta \Pi_\tau = -\int_L W^0_{j,x} X^\tau_{jik} (\zeta_i \delta\zeta_{k,x} + \zeta_{k,x} \delta\zeta_i) \,\mathrm{d}x \tag{21}$$

where the third-order tensor X^τ_{jik} stands for the geometric stiffness related to the shear stresses caused by the applied bending moment gradients—they are null for $j \neq 2, 3$ and otherwise equal to

$$X^\tau_{jik} = \frac{E}{C_{jj}} \int_S S_j(s) w_{i,s} w_k \,\mathrm{d}s \tag{22}$$

Introducing Eqs. (12), (14), (17) and (21) into (6), carrying out the integrations by parts and noting that $\delta\zeta_i$ is arbitrary, one obtains the system of dynamic equilibrium equations

$$C_{ik}\zeta_{k,xxxx} - D_{ik}\zeta_{k,xx} + B_{ik}\zeta_k - Q_{ik}\zeta_{k,xxtt} + R_{ik}\zeta_{k,tt} - X_{jik}\left(W^0_j \zeta_{k,x}\right)_{,x} + X^\tau_{jki}\left(W^0_{j,x}\zeta_k\right)_{,x} - W^0_{j,x} X^\tau_{jik}\zeta_{k,x} = 0 \tag{23}$$

One solution of the above system can be found by assuming that the free vibration motions display synchronous configurations, i.e., by considering the separation of variables

$$\zeta_k(x,t) = \phi_k(x)\, Y(t) \tag{24}$$

where $\phi_k(x)$ is a longitudinal shape function and $Y(t)$ is a time-dependent function satisfying the free vibration harmonic equation of motion $Y_{,tt} + \omega^2 Y = 0$, where ω is the angular frequency of vibration—thus, one may write

$$\zeta_{k,tt} = -\omega^2 \zeta_k \tag{25}$$

The insertion of Eq. (25) into (23) leads to the final system of equilibrium equations

$$C_{ik}\phi_{k,xxxx} - D_{ik}\phi_{k,xx} + B_{ik}\phi_k - \omega^2(R_{ik}\phi_k - Q_{ik}\phi_{k,xx}) - X_{jik}\left(W^0_j \phi_{k,x}\right)_{,x} + X^\tau_{jki}\left(W^0_{j,x}\phi_k\right)_{,x} - W^0_{j,x} X^\tau_{jik}\phi_{k,x} = 0 \tag{26}$$

which depends exclusively on derivatives with respect to x. The performance of a GBT vibration analysis involves two main tasks, namely (i) a *cross-section analysis*, to identify the GBT deformation modes and

determine the corresponding modal mechanical and mass properties and (ii) a *member analysis*, which consists of solving the ensuing vibration eigenvalue problem to obtain the member natural frequencies and associated vibration mode shapes. Next, the main aspects and operations related to the execution of each of these tasks are presented and illustrated in the context of cold-formed members (with arbitrary open cross-sections).

2.2. Cross-section analysis

The performance of a *GBT cross-section analysis* involves a sequential procedure comprising the following major steps [14,24]:

(i) Cross-section discretisation into $n+1$ *natural* nodes (ends of the n walls forming the cross-section) and m *intermediate* nodes (located within the walls)—note that, in *branched* sections (with nodes shared by more than two walls), the natural nodes are still divided into *dependent* and *independent*.
(ii) Determination of the *initial shape* functions $u_i(s)$, $v_i(s)$ and $w_i(s)$, by imposing (ii_1) unit warping displacements ($u=1$) at each independent natural node and (ii_2) unit flexural displacements ($w=1$) at each intermediate node—the cross-section *end* nodes are treated as both natural (independent or dependent) and intermediate. Note that evaluating the flexural functions $w_i(s)$ involves solving a statically indeterminate folded-plate problem (by means of the displacement method, in this work).
(iii) Calculation of the cross-section linear stiffness (13), mass (15) and geometric stiffness (18) and (22) matrices, on the basis of the initial shape functions and applied loading. One obtains fully populated matrices with components that exhibit no obvious structural meaning.
(iv) In order to uncouple the member equilibrium equation system as much as possible and, at the same time, have matrix components with clear structural meanings, one simultaneously diagonalises the linear stiffness matrices C_{ik} and B_{ik} given in Eq. (13). This leads to the cross-section *deformation modes* (the *final shape* functions $u_k(s)$, $v_k(s)$ and $w_k(s)$) and to the evaluation of the associated cross-section modal mechanical, mass and geometrical properties—several of the new matrix components have a very clear/illuminating structural meaning [14]. This process is the GBT "trademark" and makes it possible to express the equilibrium equations in *modal* form, thus leading to a fair amount of interpretation and numerical implementation advantages.

To illustrate the above concepts, Figs. 3(a) and (b) show the dimensions, elastic constants and one possible GBT discretisation of (i) a plain and (ii) a lipped channel section. On the basis of these discretisations, the GBT cross-section analysis leads to $n_d=11$ and $n_d=18$ deformation modes—the in-plane shapes of the 10 most relevant ones are given in Figs. 4(a) and (b). In either case, modes **1**–**4** are *global*: axial extension, major and minor axis bending and torsion. Then, while the plain channel section only has *local-plate* modes ($\geqslant$**5**), its lipped counterpart has both *distortional* (**5**–**6**) and *local-plate* ($\geqslant$**7**) modes.

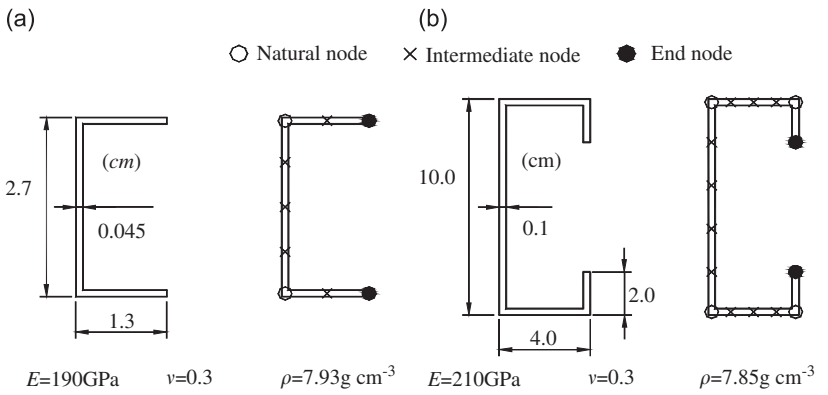

Fig. 3. Geometry and one possible GBT discretisation of (a) plain and (b) lipped channel sections.

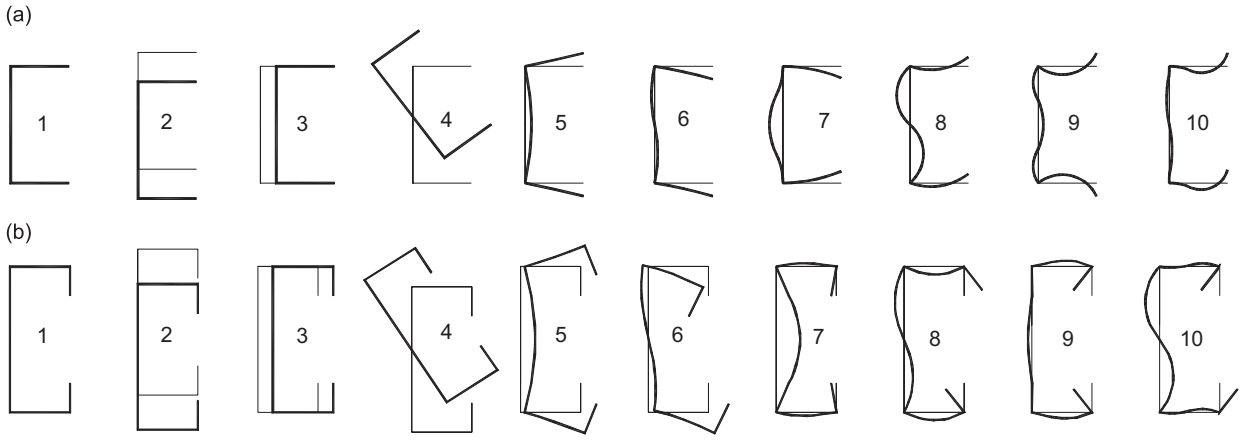

Fig. 4. In-plane shapes of the 10 most relevant deformation modes: (a) plain and (b) lipped channel.

2.3. Member analysis

The vibration eigenfunction problem to be solved is defined by Eq. (26) and the appropriate member end support conditions—indices i and k $(1, \ldots, n_d)$ now refer to the cross-section deformation modes. In the particular case of simply supported members (end sections locally/globally pinned and free to warp) either unloaded or acted by *uniform* internal forces and moments (i.e., not under stress gradients—$W^0_{j,x} = W^0_{j,xx} = 0$), the exact solutions (eigenfunctions) of this problem are of the form

$$\phi_k(x) = A_k \sin\left(n_s \pi \frac{x}{L}\right) \tag{27}$$

where A_k is the amplitude associated with deformation mode k and n_s is the vibration mode number of the solution. In members with *arbitrary* support and loading conditions, the problem is best solved (approximately) by means of a GBT-based beam finite element formulation—such a formulation was recently developed and implemented by the authors [23] in the context of stability analysis and the finite element is able to handle the influence of both (pre-buckling) longitudinal normal stress gradients and shear stresses. For the vibration analysis of loaded members, a similar finite element formulation involves the main steps and procedures that are briefly described next:

(i) Consider the variational form of the equilibrium condition (weak counterpart of Eq. (26)), given by

$$\delta V = \int_{L_e} (C_{ik}\phi_{k,xx}\,\delta\phi_{i,xx} + D_{ik}\phi_{k,x}\,\delta\phi_{i,x} + B_{ik}\phi_k\,\delta\phi_i - \omega^2(R_{ik}\phi_k - Q_{ik}\phi_{k,xx}) + W^0_j X_{jik}\phi_{k,x}\,\delta\phi_{i,x} - W^0_{j,x} X^{\tau}_{jik}(\phi_i\,\delta\phi_{k,x} + \phi_{k,x}\,\delta\phi_i))\,\mathrm{d}x = 0 \tag{28}$$

where the integrations are now carried out over the finite element length L_e, subscripts i, k identify the various deformation modes and subscript j identifies the applied stress resultant.

(ii) Approximate the modal amplitude functions $\phi_k(x)$ by means of linear combinations of standard Hermite cubic polynomials,

$$\phi_k(x) = d^e_{k.1}\psi_1(\xi) + d^e_{k.2}\psi_2(\xi) + d^e_{k.3}\psi_3(\xi) + d^e_{k.4}\psi_4(\xi) \tag{29}$$

where $d^e_{k.1} = \phi_{k,x}(0)$, $d^e_{k.2} = \phi_k(0)$, $d^e_{k.3} = \phi_{k,x}(L_e)$, $d^e_{k.4} = \phi_k(L_e)$, $\xi = x/L_e$ and

$$\Psi_1 = L_e(\xi^3 - 2\xi^2 + \xi), \quad \Psi_2 = 2\xi^3 - 3\xi^2 + 1, \quad \Psi_3 = L_e(\xi^3 - \xi^2), \quad \Psi_4 = -2\xi^3 + 3\xi^2 \tag{30}$$

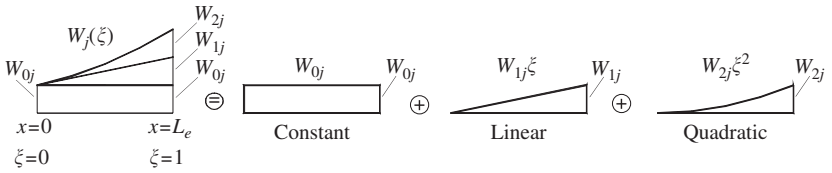

Fig. 5. Nonlinear bending moment diagram decomposition/approximation.

(iii) Assume longitudinal stress resultants for modes **2** and **3** (major and minor axis bending) of the form

$$W_j^0 = W_{0j}^0 + W_{1j}^0\xi + W_{2j}^0\xi^2 \tag{31}$$

where W_{lj}^0 is the coefficient of the lth order term of the bending moment (stress resultant associated with $j = 2$ or 3)—Fig. 5 shows the approximation achieved by means of Eq. (31), which suffices for most practical applications—recall that Hermite *cubic* polynomials are adopted to approximate $\phi_k(x)$.

(iv) Introduce Eqs. (29)–(31) into (28) and carry out the integrations over L_e, to obtain the finite element linear $\mathbf{K}^e$ and geometric $\mathbf{G}^e$ stiffness matrices, mass matrix $\mathbf{M}^e$ and modal generalised displacement vector $\mathbf{d}^e$—for members with singly symmetric cross-sections, they read

$$\mathbf{K}^e = \begin{bmatrix} \mathbf{K}^{11} & \mathbf{0} & \mathbf{0} & \mathbf{0} & \mathbf{0} & \cdots \\ & \mathbf{K}^{22} & \mathbf{0} & \mathbf{0} & \mathbf{0} & \cdots \\ & & \mathbf{K}^{33} & \mathbf{0} & \mathbf{0} & \cdots \\ & & & \mathbf{K}^{44} & \mathbf{0} & \cdots \\ & & & & \mathbf{K}^{55} & \cdots \\ \text{sym.} & & & & & \ddots \end{bmatrix}, \quad \mathbf{G}^e = \begin{bmatrix} \mathbf{0} & \mathbf{0} & \mathbf{0} & \mathbf{0} & \mathbf{0} & \cdots \\ & \mathbf{G}^{22} & \mathbf{0} & \mathbf{G}^{24} & \mathbf{G}^{25} & \cdots \\ & & \mathbf{G}^{33} & \mathbf{G}^{34} & \mathbf{G}^{35} & \cdots \\ & & & \mathbf{G}^{44} & \mathbf{G}^{45} & \cdots \\ & & & & \mathbf{G}^{55} & \cdots \\ \text{sym.} & & & & & \ddots \end{bmatrix} \tag{32}$$

$$\mathbf{M}^e = \begin{bmatrix} \mathbf{M}^{11} & \mathbf{0} & \mathbf{0} & \mathbf{0} & \mathbf{0} & \cdots \\ & \mathbf{M}^{22} & \mathbf{0} & \mathbf{M}^{24} & \mathbf{M}^{25} & \cdots \\ & & \mathbf{M}^{33} & \mathbf{0} & \mathbf{M}^{35} & \cdots \\ & & & \mathbf{M}^{44} & \mathbf{M}^{45} & \cdots \\ & & & & \mathbf{M}^{55} & \cdots \\ \text{sym.} & & & & & \ddots \end{bmatrix}, \quad \mathbf{d}^e = \begin{Bmatrix} \mathbf{d}^1 \\ \mathbf{d}^2 \\ \mathbf{d}^3 \\ \mathbf{d}^4 \\ \mathbf{d}^5 \\ \vdots \end{Bmatrix} \tag{33}$$

where the superscripts of the 4×4 sub-matrices appearing in Eqs. (32) and (33) identify the deformation modes included in the analysis. The various sub-matrix components are obtained from ($1 \leqslant p, r \leqslant 4$)

$$K_{pr}^{ik} = C_{ik}\int_0^1 \psi_{p,xx}\psi_{r,xx}\,\mathrm{d}\xi + D_{ik}\int_0^1 \psi_{p,x}\psi_{r,x}\,\mathrm{d}\xi + B_{ik}\int_0^1 \psi_p\psi_r\,\mathrm{d}\xi \tag{34}$$

$$M_{pr}^{ik} = Q_{ik}\int_0^1 \psi_{p,x}\psi_{r,x}\,\mathrm{d}\xi + R_{ik}\int_0^1 \psi_p\psi_r\,\mathrm{d}\xi \tag{35}$$

$$G_{pr}^{ik} = W_{lj}^0\left[X_{jik}^{\sigma}T_{pr}^l - \left(S_{rp}^l X_{jik}^{\tau} + S_{pr}^l X_{jki}^{\tau}\right)\right] \tag{36}$$

$$T_{pr}^l = \int_0^1 \xi^l\psi_{p,x}\psi_{r,x}\,\mathrm{d}\xi, \quad l \in \{0,1,2\}, \quad S_{pr}^l = \frac{l}{L_e}\int_0^1 \xi^{l-1}\psi_{p,x}\psi_r\,\mathrm{d}\xi, \quad l \in \{1,2\} \tag{37}$$

Taking into account the member *end support conditions*, expressed in terms of the modal degrees of freedom, one assembles the finite element matrices to obtain the (discretised) eigensystem

$$(\mathbf{K} - \mathbf{G} - \omega^2\mathbf{M})\mathbf{d} = \mathbf{0} \tag{38}$$

where ω is the angular frequency of vibration and **K**, **G**, **M** and **d** denote the global linear and geometrical stiffness matrices, mass matrix and generalised displacement vector—the components of **d** are the (unknown) GBT modal amplitudes and their derivatives.

2.3.1. GBT modal participation factors and diagrams

The solution of Eq. (38) provides the natural angular frequencies (ω) and vibration mode shapes, defined by a vector **d** that makes it possible to assess the contribution of each deformation mode, by means of the *modal participation factor* (P_k) concept. For a given GBT deformation mode k (see Fig. 4), one has

$$P_k = \frac{\int_L |\phi_k(x)|\,\mathrm{d}x}{\sum_{i=1}^{N} \int_L |\phi_i(x)|\,\mathrm{d}x} \tag{39}$$

where the numerator and denominator are the sum of the contributions of (i) that deformation mode (k) and (ii) all the N deformation modes included in the analysis to the member cross-section deformed configurations associated with the vibration mode under consideration. Although, in general, the P_i values give no information on the modal amplitude function *shapes*, the cumulative P_k vs L modal participation diagrams (e.g., see Figs. 7(b)–(d)) provide quite a good assessment of the variation of the vibration mode nature and characteristics with the member length. For instance, a member length range with $P_2+P_4 \approx 1.0$ corresponds to (major axis) flexural–torsional vibration modes—moreover, the P_2 and P_4 values indicate how relevant the mode **2** (flexure) and mode **4** (torsion) participations are in those vibration modes.

3. Illustrative example: simply supported lipped channels

The proposed GBT formulation and finite element implementation is now employed to analyse the vibration behaviour of statically loaded simply supported lipped channel beams—they are subjected to either (i) uniform bending (Fig. 6(a)) or (ii) a uniformly distributed transverse load (Fig. 6(b)), with the mid-span bending moment taken as the load parameter ($\lambda \equiv M$). The cross-section geometry and nodal discretisation are the ones displayed earlier, in Fig. 3(b). One begins by analysing the vibration behaviour of the load-free members. Then, since it is a common practice in the literature to express the static loading as a fraction of its critical buckling value, the beam buckling behaviour is studied. Finally, one investigates the vibration behaviour of loaded beams, focusing mainly on the effect of the load magnitude on the fundamental frequency value and mode shape nature.

3.1. Load-free member vibration

The curves depicted in Fig. 7(a) show the variation of the first three natural frequencies ($\omega_1 \equiv \omega_f$, ω_2 and ω_3) of the *load-free* lipped channel member with the length L (logarithmic scale). For validation purposes, some fundamental frequency (ω_f) values obtained by means of (i) ANSYS shell finite element analyses and, for

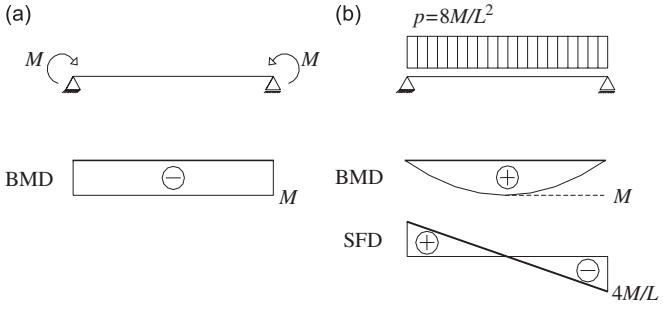

Fig. 6. Simply supported beams under (a) uniform bending and (b) a uniformly distributed load.

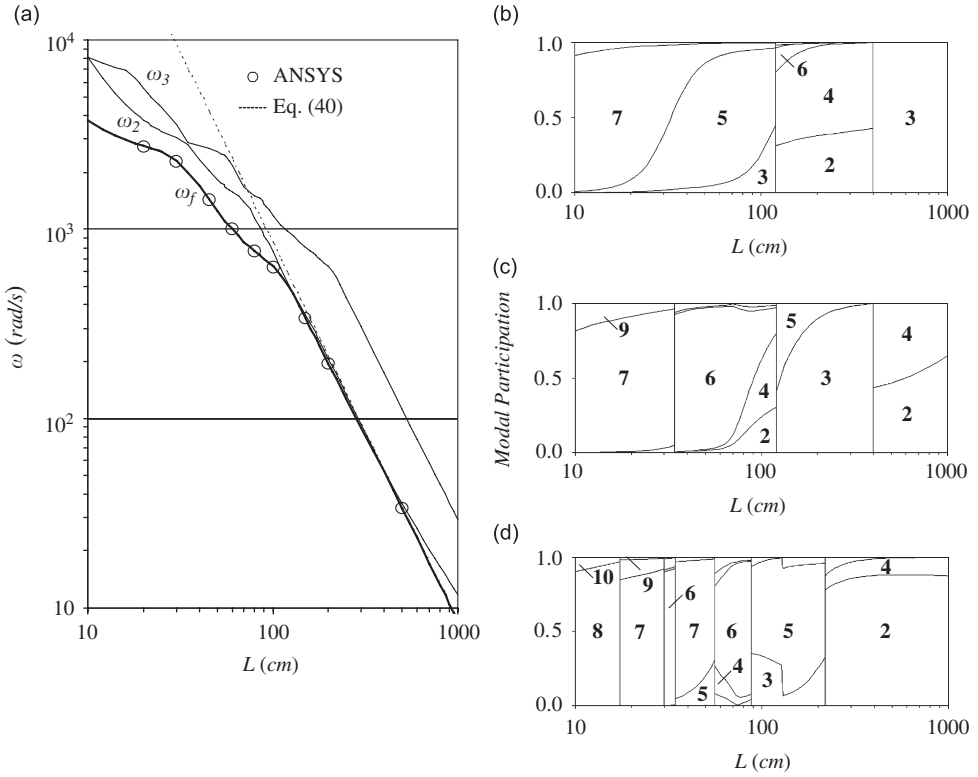

Fig. 7. Load-free member vibration behaviour: (a) variation of ω_f, ω_2 and ω_3 with L and modal participation diagrams for (b) ω_f, (c) ω_2 and (d) ω_3.

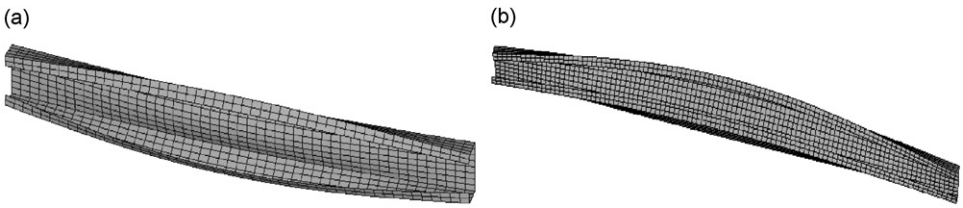

Fig. 8. Fundamental vibration mode shapes of beams with (a) $L = 100$ cm and (b) $L = 200$ cm.

(minor axis) *flexural vibration* only, (ii) the analytical expression

$$\omega_f = \left(\frac{\pi}{L}\right)^2 \sqrt{\frac{EI_3}{\rho A}} \tag{40}$$

where A and I_3 are the member cross-section area and the minor moment of inertia (e.g., Ref. [25]) are also included in Fig. 7(a). Moreover, Figs. 7(b)–(d) provide the GBT modal participation diagrams concerning the member vibration mode shapes (see Section 2.3.1)—note that the fundamental mode always exhibits a single half-wave, while the second and third ones may exhibit more than one half-wave. For illustration purposes, Figs. 8(a) and (b) show the fundamental vibration mode shapes of members with $L = 100$ and 200 cm (provided by ANSYS analyses). The observation of the vibration results presented in these figures makes it possible to draw the following conclusions:

(i) The three natural frequency values decrease monotonically with L and tend to zero as L goes to infinity. The ω_1 and ω_2 curves are very close for $150 \leqslant L \leqslant 500$ cm—moreover, they intersect at $L \approx 400$ cm, a length

for which the natures of these two vibration modes switch. For $L>400$ cm, mode **3** becomes clearly dominant, which explains why the ω_f-L curve virtually coincides with the dashed one, yielded by Eq. (40)—differences below 0.1%. Moreover, the GBT and ANSYS values agree perfectly, as the differences never exceed 2.5% (this also applies to ω_2 and ω_3, whose ANSYS values are not shown here)—note, however, that while the SFEA involve 2000–15,000 d.o.f., the GBT analyses require only about 200 (10 beam finite elements, regardless of L)—i.e., a 1%–13% fraction.

(ii) As shown by the modal participation diagram presented in Fig. 7(b), the fundamental vibration mode shape is (ii_1) *local-plate* (mode **7** predominant), for $L<25$ cm (very short beams), (ii_2) *distortional* (mode **5** governs, with relevant contributions from modes **3** and **7**—see also Fig. 8(a)), for $25<L<120$ cm, (ii_3) *flexural–torsional–distortional* (combines modes **2**, **4** and **6**—see also Fig. 8(b)), for $120<L<400$ cm and (ii_4) *purely flexural* (mode **3**), for $L>400$ cm.

(iii) The GBT modal decompositions of the second and third vibration modes, shown in Figs. 7(b) and (c), vary more with L, since they involve more deformation modes, some of them exhibiting several half-waves. For $10<L<1000$ cm, the number of participating local-plate modes increases with the vibration mode order—e.g., while only mode **7** appears in the fundamental mode, the third one involves modes **7**–**10**.

3.2. Beam buckling

The curves shown in Fig. 9(a) provide the variation of the mid-span critical moment M_{cr} with the beam length L, for the two loadings depicted in Fig. 6—also included, for validation purposes, are some shell finite element results concerning the non-uniform bending case, obtained with ANSYS (beams discretised into fine SHELL63 meshes). The modal participation diagrams displayed in Figs. 9(b) and (c) clarify the contributions of each GBT deformation mode to the beam buckling modes. After observing the results presented in these figures, one is led to the following conclusions:

(i) The uniform bending M_{cr}–L curve has a horizontal plateau ($M_{cr}\approx 3.25$ kN m) up to $L=120$ cm, followed by a descending branch. As for the non-uniform bending M_{cr}–L curve, it exhibits three zones: (i_1) an ascending branch , up to $L=80$ cm, (i_2) an almost horizontal mid-portion ($80<L\leqslant 130$ cm) tending to the uniform curve (i.e., $M_{cr}\approx 3.25$ kN m) and (i_3) a descending branch associated with lateral–torsional buckling ($L>130$ cm)—note that the reference moment depends on the beam length ($M_{cr}\propto p_{cr}L^2$), which explains why it does not decrease monotonically with L (as does the load p_{cr}).

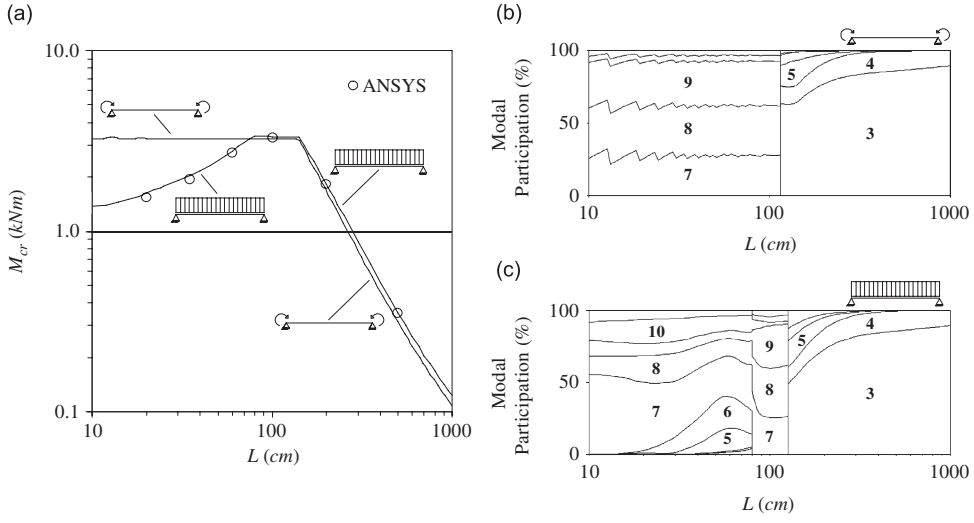

Fig. 9. Buckling behaviour of lipped channel beams under uniform and non-uniform bending: (a) M_{cr}–L curves and modal participation diagrams for (b) beams under uniform and (c) non-uniform bending.

(ii) The two M_{cr}–L curves differ by (ii$_1$) up to 60%, for $L<80$ cm, (ii$_2$) less than 4%, for $80<L\leqslant 120$ cm, and (ii$_3$) 10–15%, for $L>120$ cm. Moreover, there is an excellent agreement between the GBT-based results and the values yielded by the ANSYS analyses (the differences always below 4%).

(iii) Fig. 9(b) shows that, for $L<120$ cm, the uniformly bent beam critical buckling mode is governed by local-plate modes **7**–**9** (fairly equal contributions and up to 25 half-waves)—this explains the closeness of the two M_{cr}–L curves for $80<L\leqslant 120$ cm (i.e., the low impact of the applied moment gradients) [26]. For $L\geqslant 120$ cm, modes **3** and **4** (i.e., flexural–torsional buckling) prevail—for the lower lengths, there are also small contributions from local-plate and distortional modes (e.g., mode **5**).

(iv) Fig. 9(c) shows that, for $10<L<80$ cm, the critical buckling modes of the beams acted upon by a uniform load basically combine the local-plate modes **7**–**10**, even if non-negligible participations of the distortional modes **5** and **6** appear for $L>30$ cm and grow steadily up to $L\approx 80$ cm. Within the range $80<L<130$ cm, modes **7**–**9** exist and the mode decomposition is very similar to the uniformly bent beam one up to $L=120$ cm (see Fig. 9(b)). For $L>130$ cm, the modal composition is again very close to the uniformly bent beam one, with modes **3** and **4** playing a major role.

In order to provide a better grasp of the nature of the non-uniformly bent beam critical buckling modes (unlike those of the beam under uniform bending, they are not sinusoidal), Figs. 10(a)–(c) show the critical buckling modes of beams with (i) $L=60$ cm (local-plate/distortional buckling—see Fig. 10(a)), (ii) $L=100$ cm (local-plate buckling—see Fig. 10(b)) and (iii) $L=200$ cm (lateral–torsional buckling—see Fig. 10(c)). While the left-hand figures provide 3D representations of the ANSYS buckling modes, the ones on the right provide the amplitude functions $\phi_k(x)$ of the participating GBT deformation modes. The observation of these critical buckling mode shape representations prompts the following remarks:

(i) The $L=60$ cm beam critical buckling mode involves "diagonal" half-waves near the supports, which are due to the presence of high *shear stresses* caused by the moment gradients—Fig. 10(a) shows that these half-waves combine contributions of the GBT local-plate modes **7**–**10**, which only have meaningful amplitudes in the vicinity ($1/4L$) of each support—e.g., mode **7** exhibits a clear peak at $1/10L$ from each end support. On the other hand, the contributions of the distortional modes **5** and **6** span the whole length

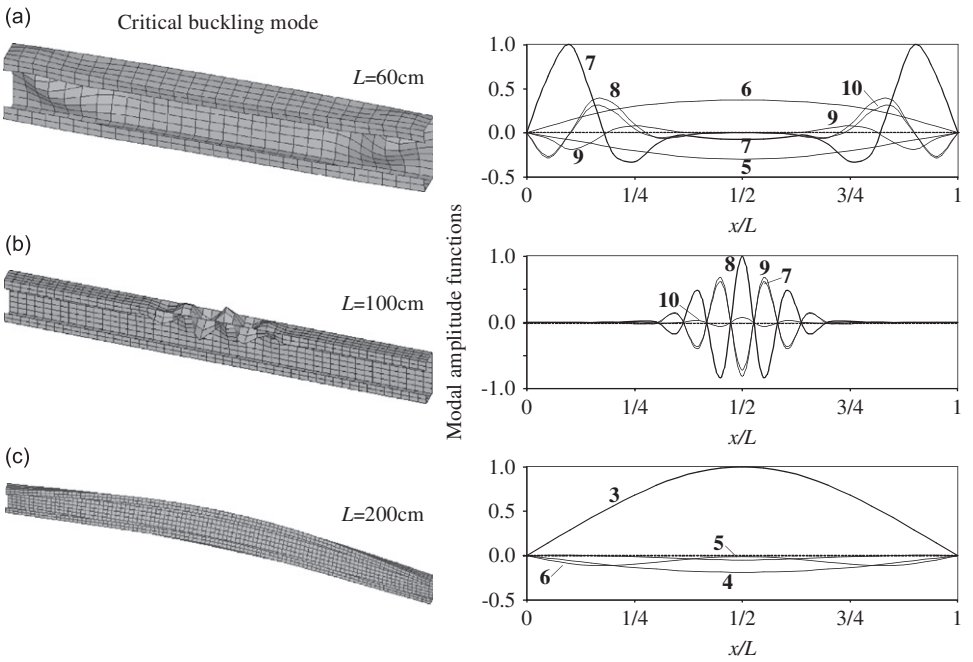

Fig. 10. Critical buckling mode representations and GBT modal amplitude functions of three non-uniformly bent beams: (a) $L=60$ cm, (a) $L=100$ cm and (c) $L=200$ cm.

and "reinforce" each other at the beam upper (compressed) flange-lip—this is why it experiences downward motions, well perceptible in Fig. 10(a).

(ii) Unlike in the previous case, the $L = 100$ cm beam critical buckling mode involves almost exclusively the central zone upper half (see Fig. 10(a)), where the deformations are due to high *longitudinal compressive stresses*. Fig. 10(b) shows the amplitude functions of the local-plate modes **7**–**10**, which display *9* unequal half-waves for $1/4 < x/L < 3/4$ (elsewhere the beams remain practically undeformed) that are not in phase (ϕ_8 and ϕ_{10} "oppose" ϕ_7 and ϕ_9) and reach all their peaks at mid-span.

(iii) Fig. 10(c) shows that, as expected, the $L = 200$ cm beam critical mode is flexural–torsional and exhibits an almost sinusoidal single half-wave—Fig. 10(c) confirms this assertion, as the amplitude functions of modes **3** and **4**, which practically account for all the critical mode shapes, are both very close to single half-wave sinusoids. However, note the small participations of modes **5** and **6**—the latter (the larger one) is null at mid-span and exhibits symmetrical maxima at $1/4L$ and $3/4L$.

3.3. Beam vibration

Finally, one investigates the vibration behaviour of the lipped channel beams—the applied load value is defined by a parameter $M^0 \equiv W_2^0$, which is taken as a given fraction (α) of its critical value, i.e., $M^0 = \alpha M_{cr}$. Figs. 11(a) and (b) demonstrate the influence of the applied loading on the beam fundamental frequency—they show curves (i) $\omega_{\alpha.u}$-L, for uniform bending, and (ii) $\omega_{\alpha.nu}$-L, for non-uniform bending (uniformly distributed load). Moreover, the modal participation diagrams presented in Fig. 12 (for both loading cases and five load levels: $\alpha = 0$, 0.1, 0.5, 0.95, 0.999) provide in-depth information on the evolution of the beam fundamental vibration mode shape as the applied load level increases. Finally, Figs. 13(a)–(c) show the variation of the frequency ratios $\omega_{\alpha.u}/\omega_{\alpha=0}$, $\omega_{\alpha.nu}/\omega_{\alpha=0}$ and $\omega_{\alpha.nu}/\omega_{\alpha.u}$ with α, for beams with lengths $L = 30$, 70, 120 and 200 cm—they reveal the load sensitivity of the beam fundamental frequency. After observing the results presented in these figures, the following conclusions can be drawn:

(i) Figs. 11(a) and (b) show that, for both loading cases, the presence of bending moments only causes noticeable fundamental frequency drops for $\alpha \geqslant 0.25$. Within the $0.5 < \alpha < 0.95$ applied moment range, the frequency drop rate increases significantly in both cases. Moreover, for $\alpha \geqslant 0.95$ the curves cease to descend monotonically, as they exhibit more or less pronounced upward branches for some small and intermediate length ranges—this stems from the increasing number of half-waves displayed by the corresponding vibration modes.

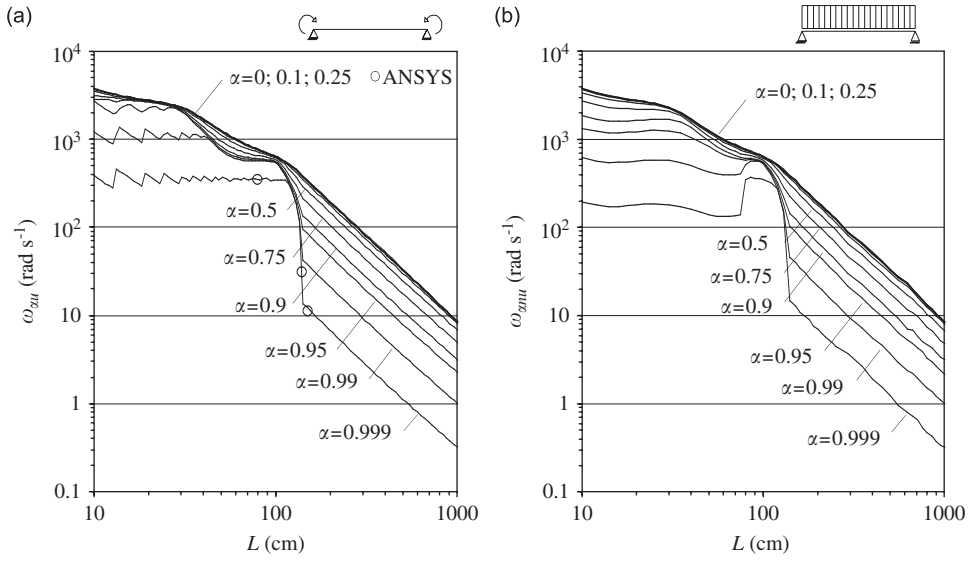

Fig. 11. (a) $\omega_{\alpha.u}$–L and (b) $\omega_{\alpha.nu}$–L curves for $\alpha = 0$, 0.1, 0.25, 0.5, 0.75, 0.9, 0.95, 0.99, 0.999.

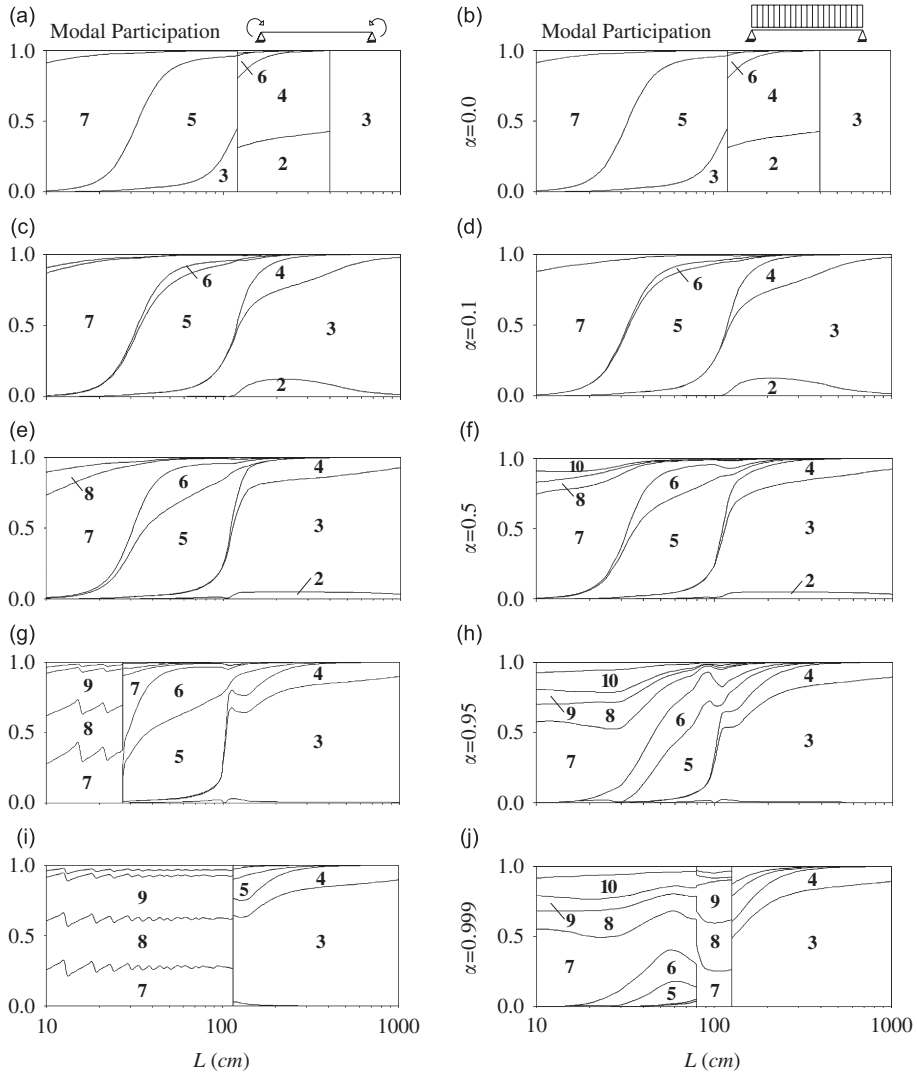

Fig. 12. Modal participation diagrams for (a)–(b) $\alpha = 0$, (c)–(d) $\alpha = 0.1$, (e)–(f) $\alpha = 0.5$, (g)–(h) $\alpha = 0.95$ and (i)–(j) $\alpha = 0.999$.

(ii) In both cases, severe fundamental frequency drops (88% and 86%) occur for $110 \leqslant L \leqslant 145$ cm—within this short length range, the vibration mode changes abruptly from local (**7–9**) with 25 half-waves to flexural–torsional–distortional (**3–6**) with a single half-wave, i.e., a much more flexible configuration. In order to confirm this particular behaviour, the three ANSYS values included in Fig. 11(a) were calculated—a very good agreement was found, both in terms of the frequency values and the corresponding vibration mode shapes (not shown).

(iii) The comparison between the modal participation diagrams shown in Figs. 12(a)–(c) and 12(b)–(d) shows that, unlike the ω_f value, the fundamental vibration mode shape may be considerably altered by the presence of even quite small applied moments ($\alpha = 0.1$)—in fact, either the distortional mode **6** joins modes **5** and **7** (intermediate beams) or the global mode **3** join modes **2** and **4** (longer beams—they are totally separated for $\alpha = 0$). Within the $0.1 < \alpha < 0.95$ range (see Figs. 12(e) and (f)), modes **8–10** progressively replace mode **7** (short beams), the contributions of modes **5** and **6** become closer (intermediate beams) and the relevance of mode **2** gradually fades (longer beams). Finally, for $\alpha \geqslant 0.95$ the vibration mode shapes change quite drastically, approaching their corresponding critical buckling

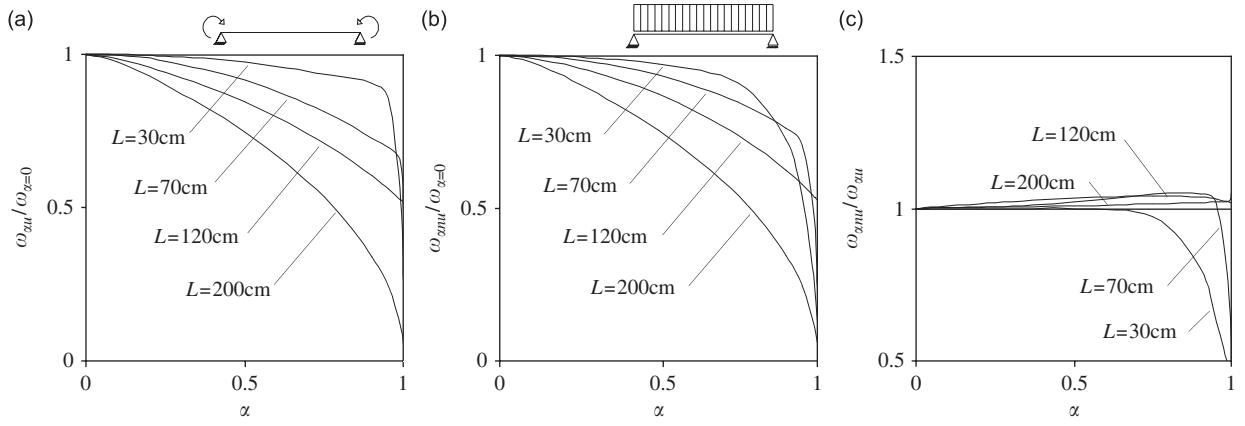

Fig. 13. Variation of the frequency ratios concerning four beam lengths: (a) $\omega_{\alpha.u}/\omega_{\alpha=0}$ in uniformly bent beams, (b) $\omega_{\alpha.nu}/\omega_{\alpha=0}$ in non-uniformly bent beams and (c) the relation between the two ($\omega_{\alpha.nu}/\omega_{\alpha.u}$).

mode counterparts (see Figs. 12(g)–(j))—for $\alpha = 0.999$, the beam fundamental vibration and critical buckling modes virtually coincide throughout the whole length range, as shown by Figs. 12(i) and (j) and 9(b) and (c)).

(iv) Figs. 13(a) and (b) show that the variation of the fundamental frequency drop with α clearly depends on L—although all the $\omega_\alpha/\omega_{\alpha=0} - \alpha$ curves have unit values and null derivatives at $\alpha = 0$, the ones associated with higher lengths exhibit lower $\omega_\alpha/\omega_{\alpha=0}$ values within the range $0<\alpha<0.8$–0.95, which means that the load sensitivity of the fundamental frequency increases with the length. As the loadings approach their critical levels ($\alpha\to 1$), the ratio $\omega_\alpha/\omega_{\alpha=0}$ drops to zero—however, the curves associated with intermediate lengths ($L = 70$ and 120 cm) exhibit higher values.

(v) From Fig. 13(c) one can assess the effect of the moment gradients on the load sensitivity of the beam fundamental frequencies, quantified by the ratio $\omega_{\alpha.nu}/\omega_{\alpha.u}$. Looking at the plot $\omega_{\alpha.nu}/\omega_{\alpha.u} - \alpha$, one realises that this effect is negligible for $\alpha<0.75$ ($\omega_{\alpha.nu}/\omega_{\alpha.u}\approx 1$) and for the two longer beams ($L = 120$ and 200 cm), regardless of α. For the higher load levels, $L = 30$ and 70 cm curves exhibit drops going up to about 0.5, which shows that the moment gradients may lead to significantly *more flexible* vibration modes—this stems from the qualitative differences between the buckling modes of the two pairs of shorter beams (see Figs. 9(b) and (c)).

(vi) Finally, one last word about the difference between the vibration behaviours of the uniformly bent beams and compressed columns (the latter studied in Ref. [20]). For small load levels ($\alpha<0.25$), while the columns experience noticeable (although small) frequency drops and no vibration mode shape change, the beams have marginal frequency drops and quite substantial vibration mode shape changes. For higher load levels, however, both the column and the beam vibration mode shapes tend to their buckling mode counterparts—while the column changes concern only the number of half-waves, the beam ones are much more dramatic.

4. Illustrative example: plain channel cantilevers

One now analyses the vibration behaviour of statically loaded plain channel (U-section) cantilevers loaded as shown in Fig. 14(a)—they are subjected to two tip transverse and axial (compressive) point loads, which give the linear bending moment and uniform shear/axial force diagrams, depicted in Figs. 14(b) and (c). The magnitudes of the two loads are $Q_z = 0.2\lambda$ and $P = \lambda$, where λ is the (single) load parameter. The cross-section geometry and discretisation are those already shown in Fig. 3(a). In the next sub-sections, one addresses the cantilever load-free vibration, buckling and loaded vibration behaviours—the load-free vibration analysis includes a detailed comparison with the experimental and numerical (SFEA) results reported by Klausbruckner and Pryputniewicz [4].

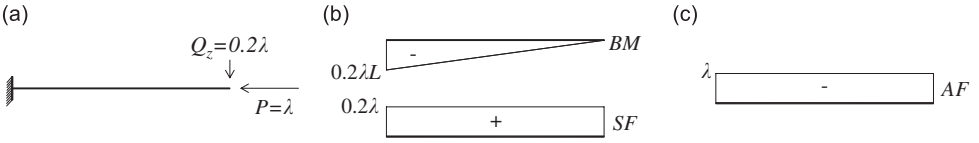

Fig. 14. Cantilever loading: (a) acting forces and (b)–(c) corresponding internal force diagrams.

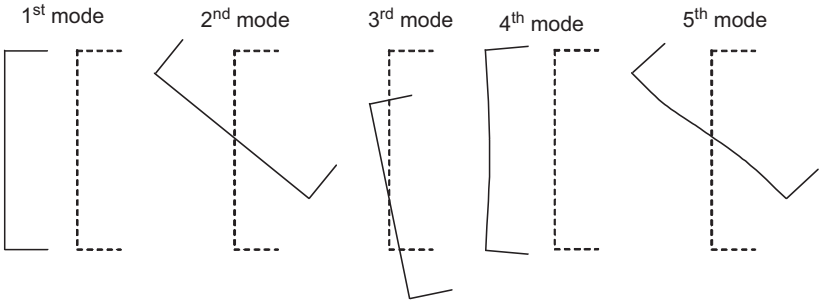

Fig. 15. Cantilever I: end section-deformed configuration for the first five vibration modes.

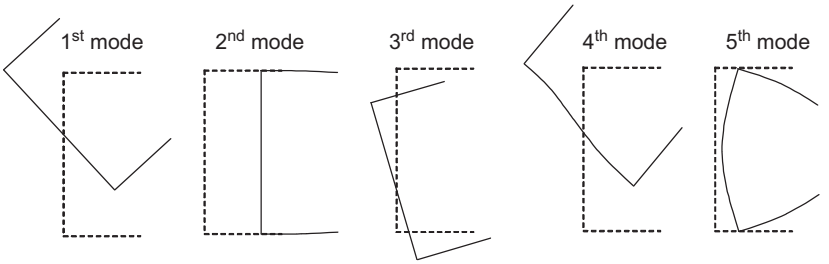

Fig. 16. Cantilever II: end section-deformed configuration for the first five vibration modes.

4.1. Load-free vibration—comparison with experimental results

Three cantilevers with material properties $E = 190\,\text{GPa}$, $\nu = 0.3$ and $\rho = 7.93 \times 10^{-3}\,\text{g mm}^{-3}$, and almost identical geometries ($L = 29.5\,\text{cm}$, $b_w = 2.7\,\text{cm}$ and $h = 4.5\,\text{cm}$—they only differ in the flange width b_f) are analysed. They are hereafter designated as Cantilever I ($b_f = 0.6\,\text{cm}$), Cantilever II ($b_f = 1.3\,\text{cm}$) and Cantilever III ($b_f = 3.2\,\text{cm}$), and were *experimentally* and *numerically* studied by Klausbruckner and Pryputniewicz [4]. These authors chose these rather small length and cross-section dimensions because of the methodology employed to perform the tests: laser hologram interferometry—the "small cantilevers" are excited acoustically and displacement amplitudes at several points located on their walls are memorised by the holographic equipment, through optical wavefronts, making it possible to obtain a set of holograms providing information about the vibration mode shapes and the corresponding natural frequency values.

The GBT analyses adopted cantilever longitudinal discretisations into 10 beam finite elements and the results presented in Tables 1–3 (Cantilevers I, II and III) consist of estimates of the 10 first natural frequencies (in Hz), obtained (i) *experimentally* (ω_{EXP}) and *numerically* (ω_{FEM}) by Klausbruckner and Pryputniewicz and (ii) by means of GBT analyses (ω_{GBT} and modal participation diagrams of some vibration modes)—they also include the values of the natural frequency ratios $\varepsilon_{\text{EXP}} = \omega_{\text{EXP}}/\omega_{\text{GBT}}$ and $\varepsilon_{\text{FEM}} = \omega_{\text{FEM}}/\omega_{\text{GBT}}$. These results are also depicted graphically: while Figs. 18–20 provide the modal amplitude functions $\phi_k(x)$ associated with the first five vibration modes of Cantilevers I–III, Figs. 15–17 show the deformed configurations of the

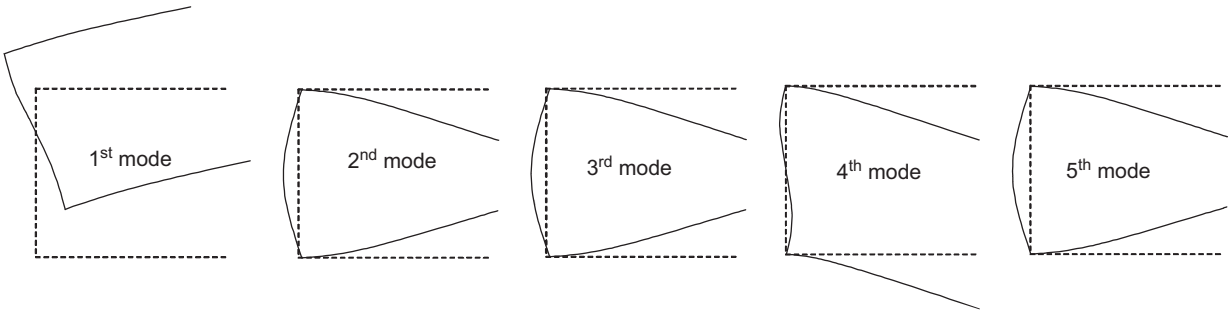

Fig. 17. Cantilever III: end section-deformed configuration for the first five vibration modes.

Table 1
Experimental and numerical results concerning the vibration behaviour of Cantilever I

Vibr. mode	Klausbruckner		GBT			Modal participation (%)								Configuration	
	ω_{EXP}	ω_{FEM}	ω_{GBT}	ε_{EXP}	ε_{FEM}	2	3	4	5	6	7	8	9	Mode	n_s
1	55.1	57.9	53.2	1.04	1.09	0	99.7	0	0.3	0	0	0	0	F	1
2	102.1	102.9	101.8	1.00	1.01	3.1	0	96.9	0	0	0	0	0	T	1
3	314.7	321.8	322.4	0.98	1.00	77.2	0	22.3	0	0.5	0	0	0	FT	1
4	337.7	354.8	329.5	1.02	1.08	0	94.3	0	5.5	0	0.2	0	0	F	2
5	446.8	453.9	437.5	1.02	1.04	4.1	0	95.0	0	0.7	0	0.2	0	T	2
6	861.9	887.6	847	1.02	1.05	0	64.7	0	34.1	0	1.2	0	0	FLP	3
7	1113.9	1147.9	1101.8	1.01	1.04	1.1	0	94.5	0	3.2	0	1.2	0	T	3
8	1335.9	1320.4	1304.7	1.02	1.01	0	29.0	0	68.6	0	2.3	0	0.1	FLP	4
9	1624.3	1576.0	1582.4	1.03	1.00	0	13.4	0	83.0	0	3.5	0	0.1	FLP	5
10	1842.8	1782.0	1827.6	1.01	0.98	0	7.6	0	87.3	0	4.9	0	0.2	FLP	6

Table 2
Experimental and numerical results concerning the vibration behaviour of Cantilever II

Vibr. mode	Klausbruckner		GBT			Modal participation (%)								Configuration	
	ω_{EXP}	ω_{FEM}	ω_{GBT}	ε_{EXP}	ε_{FEM}	2	3	4	5	6	7	8	9	Mode	n_s
1	117.3	119.0	119.6	0.98	0.99	9.6	0	88.7	0	1.7	0	0	0	T	1
2	–	131.9	131.3	–	1.00	0	98.0	0	2.0	0	0	0	0	F	1
3	409.2	413.8	422.7	0.97	0.98	66.0	0	29.5	0	4.5	0	0	0	FT	1
4	628.9	638.5	648.1	0.97	0.99	6.0	0	64.0	0	30.0	0	0	0	TLP	2
5	730.6	725.6	733.7	1.00	0.99	0	37.1	0	60.4	0	2.5	0	0	FLP	2
6	941.7	889.5	896.4	1.05	0.99	0	14.4	0	84.1	0	1.5	0	0	FLP	1
7	975.7	930.9	939.1	1.04	0.99	0	9.1	0	89.8	0	1.0	0	0	FLP[a]	3
8	1071.9	1027.3	1041.6	1.03	0.99	0	25.0	0	71.4	0	3.5	0	0.1	FLP[a]	3
9	1101.5	1058.6	1074.9	1.02	0.98	0	9.6	0	89.0	0	1.4	0	0	FLP	4
10	1242.6	1194.7	1219.6	1.02	0.98	0	3.2	0	95.9	0	0.8	0	0.1	LP	5

[a]Although the seventh and eight vibration modes exhibit very similar characteristics, they differ in the signs of the modal amplitude functions ϕ_3 and ϕ_5, which are the same in the first case and opposite in the second one.

corresponding free end sections. On the basis of the comparison between the three sets of vibration results, one draws the following conclusions:

(i) The ε_{EXP} values have an average and standard deviation equal to 1.01 and 0.02 (Cantilever I) 1.01 and 0.03 (Cantilever II), and 1.00 and 0.02 (Cantilever III). Moreover, the differences never exceed 5%

Table 3
Experimental and numerical results concerning the vibration behaviour of Cantilever III

Vibr. mode	Klausbruckner		GBT			Modal participation (%)								Configuration	
	ω_{EXP}	ω_{FEM}	ω_{GBT}	ε_{EXP}	ε_{FEM}	2	3	4	5	6	7	8	9	Mode	n_s
1	117.5	119.5	119.9	0.98	1.00	12.5	0	39.6	0	47.9	0	0	0	FTLP	1
2	231.1	222.2	224.7	1.03	0.99	0	1.7	0	98.3	0	0	0	0	LP	1
3	259.5	252.0	255.0	1.02	0.99	0	0.6	0	99.4	0	0	0	0	LP	2
4	311.6	300.3	306.1	1.02	0.98	0.8	0	1.7	0	97.5	0	0	0	ALP	2
5	312.0	307.8	312.3	1.00	0.99	0	0.3	0	99.5	0	0.2	0	0	LP	3
6	329.7	331.0	334.2	0.99	0.99	0	79.6	0	17.8	0	2.6	0	0	FLP	1
7	–	360.4	368.2	–	0.98	0.3	0	0.5	0	99.0	0	0.2	0	ALP	3
8	391.4	386.5	394.8	0.99	0.98	0	0	0	99.5	0	0.3	0	0.2	LP	4
9	445.9	433.1	445.4	1.00	0.97	1.0	0	0.6	0	98.1	0	0.3	0	ALP	4
10	490.7	486.7	501.2	0.98	0.97	0	0	0	99.3	0	0.5	0	0.2	LP	5

and are higher than 3.0% only in 5 cases (out of 28). As for the ε_{FEM} values, they have an average and standard deviation equal to 1.03 and 0.04 (Cantilever I), 0.99 and 0.01 (Cantilever II) and 0.98 and 0.01 (Cantilever III)—with just two exceptions, the differences are always below 5% and larger than 3.0% only in three of the remaining 28 cases.

(ii) The two exceptions mentioned in the previous item (differences of 9% and 8%) concern the first and fourth vibration modes of Cantilever I (“narrow” flanges)—in both cases, one has minor axis flexural vibration modes exhibiting either one (first mode) or two (fourth mode) half-waves (see Figs. 15 and 18). Since no plausible explanation was found for this discrepancy, it was decided to perform a FEM vibration analysis in ABAQUS, adopting S4 shell element discretisations similar to the ones of Klausbruckner and Pryputniewicz [4]—the values obtained ($\omega_f = 53.1$ Hz and $\omega_4 = 329.2$ Hz) virtually coincide with those yielded by the GBT analyses. On the other hand, the application of classical beam vibration theory (e.g., Ref. [25]) leads to the analytical expressions:

$$\omega_{n_s=1} = \left(\frac{1.8751}{L}\right)^2 \sqrt{\frac{EI_3}{\rho A}} \quad \omega_{n_s=2} = \left(\frac{4.6941}{L}\right)^2 \sqrt{\frac{EI_3}{\rho A}} \tag{41}$$

for the natural frequencies corresponding to minor axis flexural vibration modes with one and two half-waves (I_3 is the minor axis moment of inertia)—for the cases under consideration, Eq. (41) yield $\omega_f = \omega_{n_s=1} = 53.2$ Hz and $\omega_4 = \omega_{n_s=2} = 333.2$ Hz, values that are very close to both the ABAQUS and GBT-based ones (in the second case, the GBT-based estimate is slightly lower than the values yielded by Eq. (41b), due to a very small participation of the local-plate deformation mode **5**). Thus, one may conclude that the two FEM estimates reported by Klausbruckner and Pryputniewicz are not very accurate—even if no logical explanation was found for this fact.

(iii) There are two natural frequencies (second of Cantilever II and seventh of Cantilever III) that correspond to minor axis flexural vibration modes not obtained experimentally. However, the FEM and GBT-based values compare very well in both cases—$\varepsilon_{FEM} = 1.00$ and $\varepsilon_{FEM} = 0.98$.

(iv) As the flange width increases (Cantilever I → Cantilever III), the ω_{GBT} values tend to overestimate ω_{EXP} and ω_{FEM} slightly further. In order to retain the accuracy of the GBT-based estimates, it would be necessary to include more intermediate nodes in the flanges (finer cross-section discretisation).

(v) Even in the case of the higher-order natural frequencies, the GBT-based estimates are rather accurate—note that the ε_{EXP} and ε_{FEM} values are always of the same order of magnitude.

(vi) In all three cantilevers, the *local-plate* deformation modes (**5**–**9**) become more relevant as both b_f and the vibration mode order increase—indeed, the contributions of these deformation modes are more relevant for vibration modes of order equal to or higher than *six* (Cantilever I—$b_f = 6$ mm), *four* (Cantilever II—$b_f = 13$ mm) and *one* (Cantilever III—$b_f = 27$ mm).

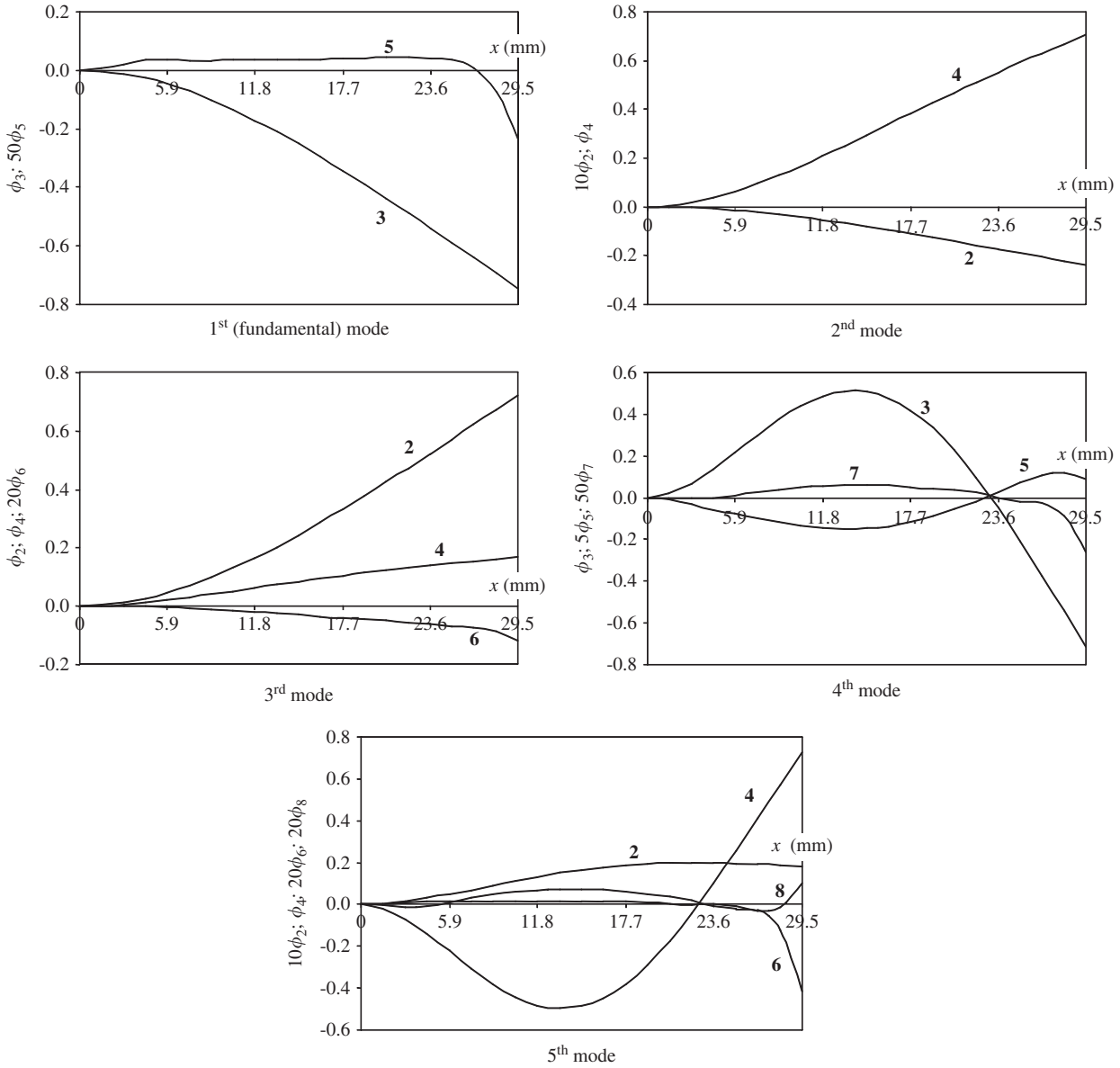

Fig. 18. Cantilever I: modal amplitude functions $\phi_k(x)$ concerning the first five vibration modes.

(vii) The accuracy of the results provided by the classical beam vibration theories depends on the member *geometry* (cross-section dimensions) and *order* of the vibration mode—indeed, none of the natural frequencies yielded by GBT vibration analyses of Cantilever III that include only the rigid-body modes (**2**–**4**) is accurate.

(viii) The relevance of torsion mode **4** *decreases* with b_f—indeed, it participates in 4 (Cantilever I), 3 (Cantilever II) and 1 (Cantilever III) of the first ten vibration modes. This is because a b_f increase fosters a warping stiffness rise much larger than its in-plane deformation counterpart.

(ix) In Cantilever III, the local-plate deformation modes (**5**–**9**) are dominant, as the rigid-body modes (**2**–**4**) only contribute to the first and sixth vibration modes. Note also the existence of a local-plate vibration mode with an anti-symmetric cross-section configuration (fourth mode—see Fig. 17), a feature

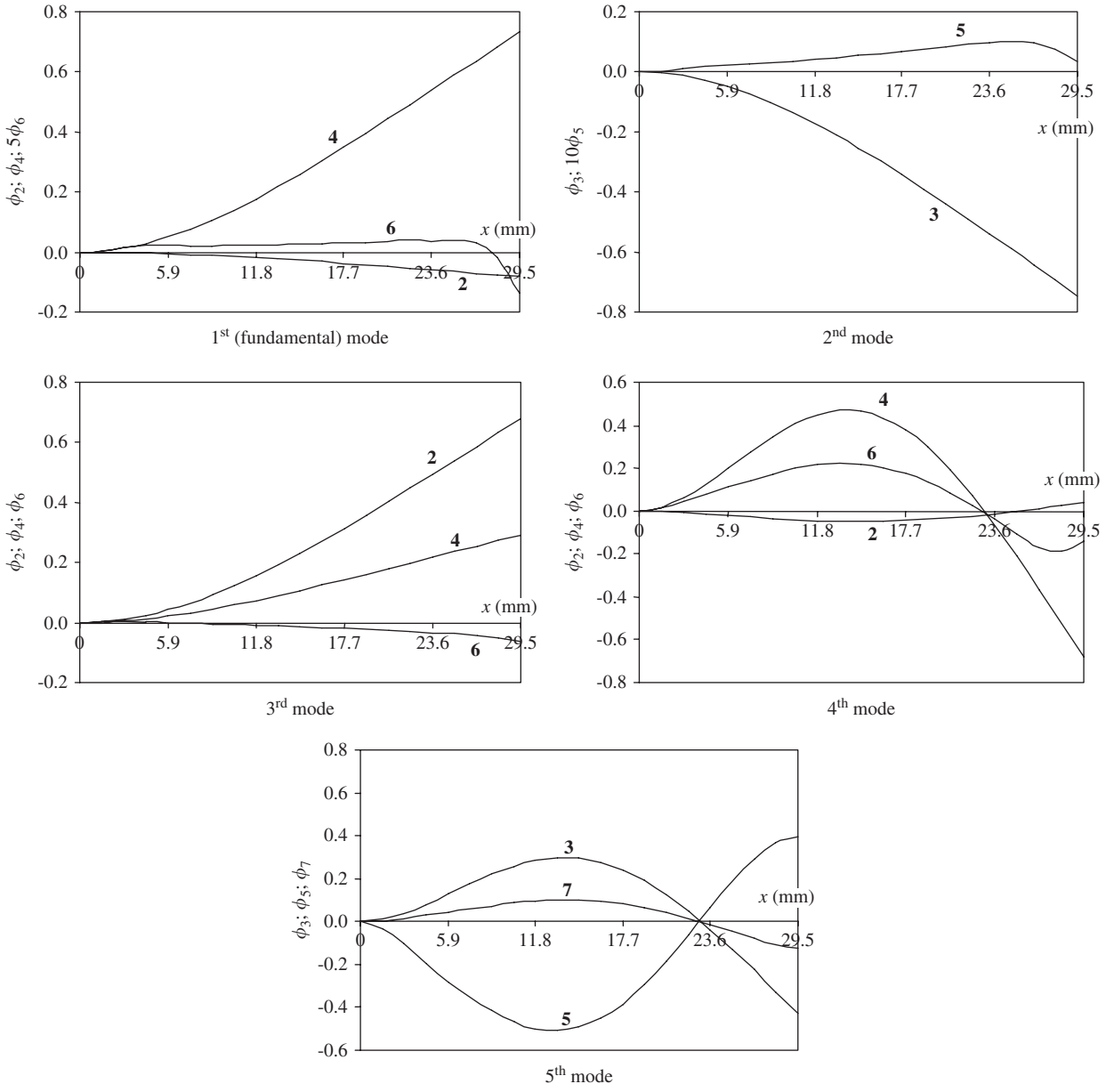

Fig. 19. Cantilever II: modal amplitude functions $\phi_k(x)$ concerning the first five vibration modes.

that never occurs in Cantilevers I and II. Using finite strip analysis, Cheung and Cheung [27] showed that, in members with several walls, such modes may be associated with lower-order natural frequencies.

(x) No conclusion could be obtained concerning the number of half-waves exhibited by a given vibration mode—i.e., how the flange width and/or the vibration mode order influence it.

4.2. *Load-free vibration—variation with the length*

Figs. 21(a) and (b) concern cantilevers with type II cross-section and display (i) ω–L curves concerning the first five vibration modes and (i) the GBT modal participation diagram of the fundamental one—also included

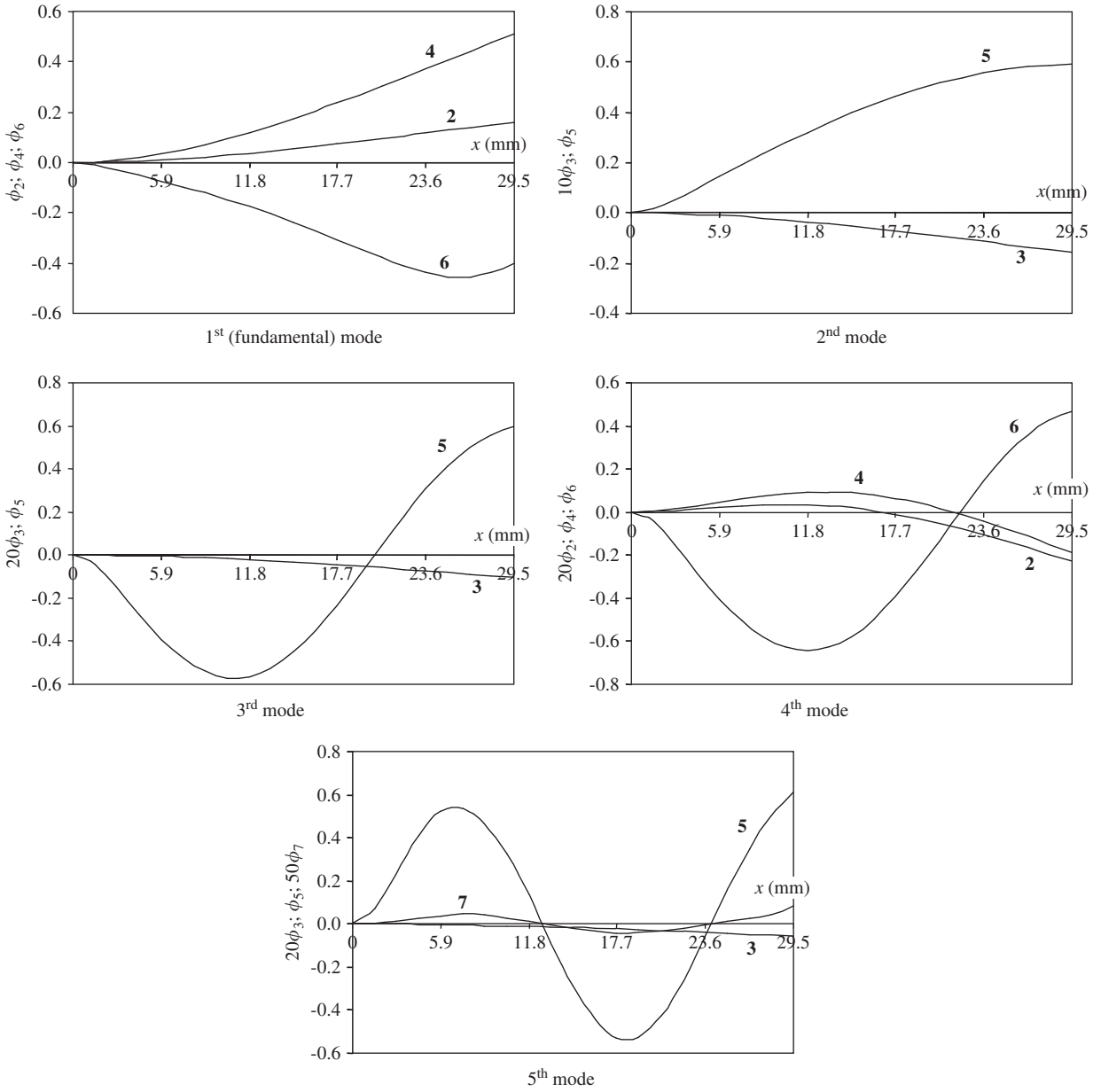

Fig. 20. Cantilever III: modal amplitude functions $\phi_k(x)$ concerning the first five vibration modes.

in Fig. 21(a) are a few fundamental frequency values determined by means of ANSYS SFEA. The observation of all these vibration results leads to the following comments:

(i) The five ω–L curves decrease monotonically with L and exhibit several distinct branches. For ω_1 (fundamental frequency), one has (i_1) an initial nonlinear branch, for $L \leqslant 10\,\text{cm}$, ($i_2$) an intermediate linear branch, for $10 < L < 40\,\text{cm}$ and (i_3) a last branch, still linear but slightly steeper, for $L > 40\,\text{cm}$. Note that there is a virtually perfect match between the ANSYS and GBT-based ω_1 values, even if the GBT analyses involve between 2% and 20% of number of degrees of freedom required by the SFEA.

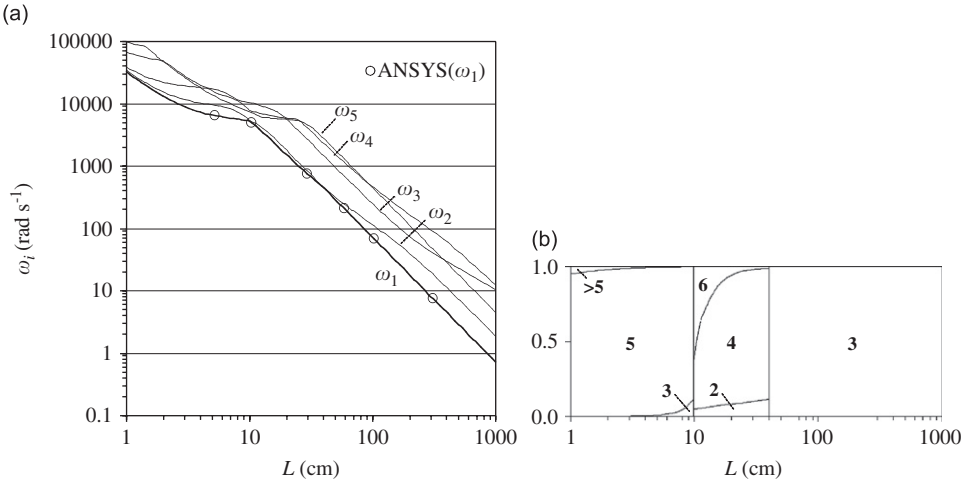

Fig. 21. Cantilever (a) first five ω–L curves and (b) fundamental mode participation diagram.

(ii) The four remaining curves (ω_2–L to ω_5–L) follow the same qualitative trend as their fundamental counterpart. Note, however, that the initial nonlinear branch becomes more "complex" as the vibration mode order increases.

(iii) The modal participation diagram shows that the cantilever fundamental vibration modes either (iii_1) are governed by the local-plate mode **5**, with small contributions of the other local-plate modes ($>$**5**) or mode **3** ($L<10$ cm), (iii_2) combine modes **2**, **4** and **6** ($10<L<40$ cm—*flexural–torsional–distortional* vibration) or (iii_3) involve only mode **3** ($L>40$ cm). Like in the lipped channel beams (see Fig. 7(b)), (iii_1) the participation diagram exhibits two "abrupt" transitions ($L=10$ and 40 cm) and (iii_2) the odd- and even-numbered GBT deformation modes never mix in a vibration mode (singly symmetric section).

4.3. Cantilever buckling

The buckling behaviour of cantilevers acted upon by the single-parameter loading shown in Fig. 14(a), combining tip transverse (0.2λ) and axial loads (λ), is now investigated. Figs. 22(a) and (b) provide the λ_{cr}–L curve and the modal participation diagram of the critical buckling mode—as before, some ANSYS shell finite element results are also included for the sake of validation. After observing these buckling results, one readily concludes that:

(i) The λ_{cr}–L curve descends monotonically and has three distinct branches: (i_1) a nonlinear branch with a decreasing slope, for $L\leqslant 7$ cm, (i_2) a first linear branch with a moderate slope, for $7<L<45$ cm and (i_3) a second linear branch (steeper than the previous one), for $L>45$ cm—note the qualitative similarity between curves λ_{cr}–L and ω_1–L. Moreover, there is again a virtual coincidence between the ANSYS and GBT-based critical buckling load values.

(ii) For $L<45$ cm, the cantilever critical buckling modes combine dominant local-plate modes **5** and **6** (with participations varying with L), together with a small contribution of higher-order local-plate modes ($>$ **6**) and global modes **3** and **4** (only for $7<L<45$ cm). On the other hand, the longer cantilevers ($L>45$ cm) buckle in a combination of modes **3** and **4** (*lateral–torsional* buckling—the participation of mode **3** grows significantly with L), in a few cases with a tiny bit of mode **2**.[3] Note that the buckling occurs in either single half-wave modes ($L<7$ cm or $L>45$ cm) or modes with 2–9 half-waves ($7<L<45$ cm), although this information is not available in Fig. 22(b).

[3]Since this is a "beam-column type" cantilever, its global buckling behaviour combines (i) flexural–torsional buckling (modes **2** and **4**) or minor axis flexural buckling (mode **3**), both associated with the column behaviour with (ii) lateral–torsional buckling (modes **3** and **4**), associated with the beam behaviour.

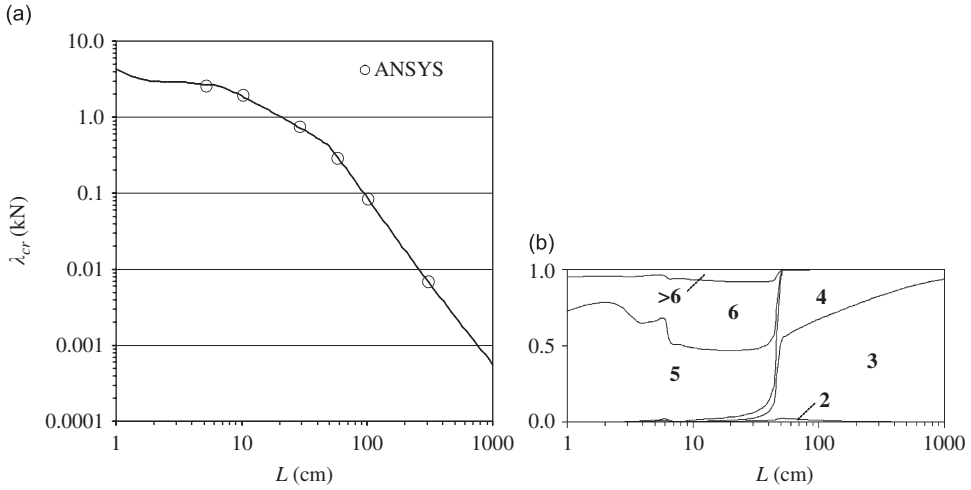

Fig. 22. Cantilever buckling behaviour: (a) λ_{cr}–L curve and (b) critical mode participation diagram.

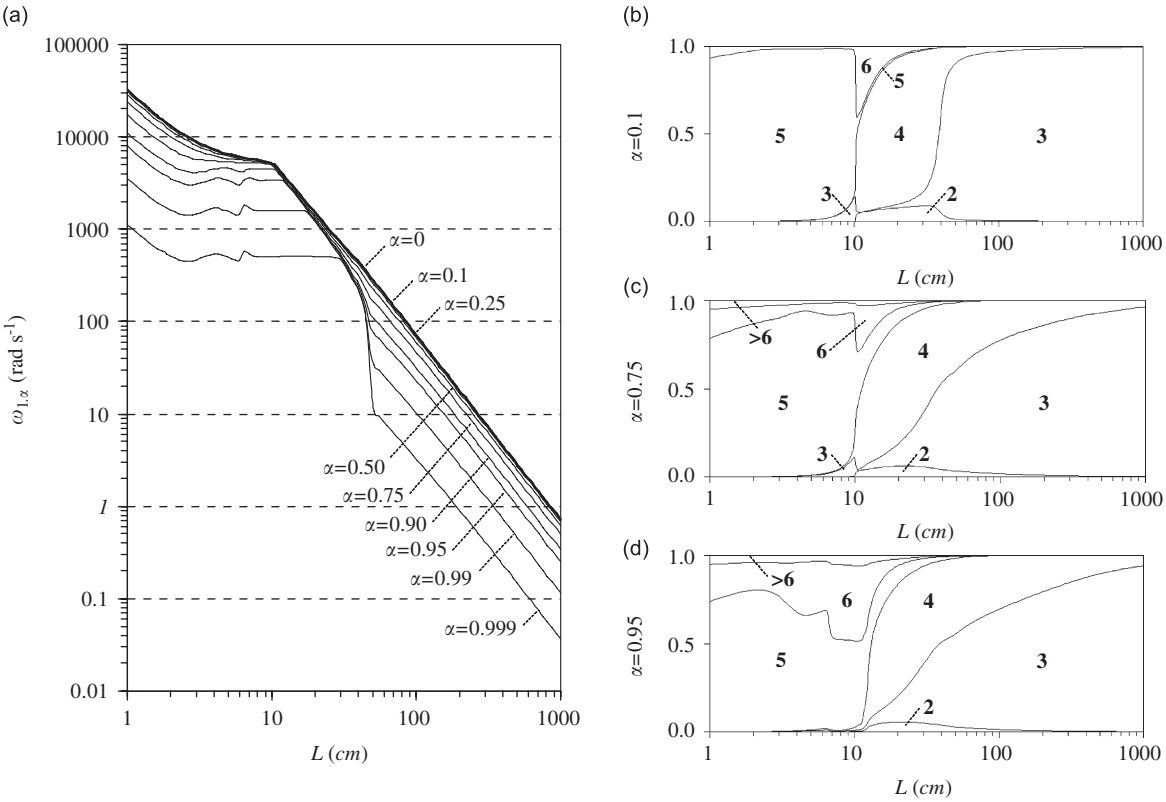

Fig. 23. Cantilever beam column (a) ω_1–L curves (for nine different α values) and (b) modal participation diagrams for (b) $\alpha = 0.1$, (c) $\alpha = 0.75$ and (d) $\alpha = 0.95$.

4.4. Cantilever vibration

Finally, one investigates the loaded cantilever vibration behaviour, where the applied loading is defined by a fraction of its critical value ($\lambda = \alpha\lambda_{cr}$). While Fig. 23(a) shows the variation of the cantilever beam-column fundamental frequency ω_1 with α (9 different values are dealt with), Figs. 23(b)–(d) display the modal

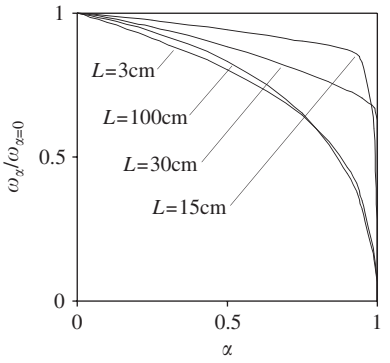

Fig. 24. Variation of $\omega_\alpha/\omega_{\alpha=0}$ with α for cantilevers with $L = 3$, 15, 30 and 100 cm.

participation diagrams of the fundamental vibration mode for $\alpha = 0.1$, 0.75 and 0.95. As for Fig. 24, it provides the variation of the ratio $\omega_\alpha/\omega_{\alpha=0}$ with α for beams with lengths $L = 3$,[4] 15, 30 and 100 cm. The observation of these vibration results prompts the following remarks:

(i) For $\alpha \geqslant 0.5$, the loading causes noticeable fundamental frequency drops for $L \leqslant 10$–30 cm and $L \geqslant 40$–55 cm (the limits vary with α)—this drop is almost imperceptible for $10\text{–}30 \leqslant L \leqslant 40\text{–}55$ cm.
(ii) For $\alpha \geqslant 0.9$, the ω_1–L curves no longer descend monotonically in the small length range ($L \leqslant 10$–30 cm), whereas they remain fairly linear and parallel (below) to the load-free vibration one for $L \geqslant 40$–55 cm. The ω_1 drops become quite drastic as one approaches the critical loading ($\alpha \geqslant 0.95$).
(iii) The comparison between Figs. 23(b) ($\alpha = 0.1$) and 21(b) ($\alpha = 0$) shows that, unlike the ω_1 value, the vibration mode shape may be considerably altered by the presence of even a small loading (10% of the critical one)—e.g., since the bending moments *couple* the GBT deformation modes, the participation diagram transitions occurring for $L = 10$ and 40 cm cease to be "abrupt". Moreover, this small loading affects mostly the fundamental vibration mode shapes of cantilevers with intermediate lengths ($10 < L < 100$ cm), as they now combine all the modes **2**–**6** in varying proportions—the shorter ($L < 10$ cm) and longer ($L \geqslant 100$ cm) cantilevers continue to vibrate in "almost pure" local-plate and "pure" flexural modes, due to the minute bending moments and low stiffness, respectively.
(iv) Figs. 23(c) and (d) show that the fundamental vibration mode participation diagram tends to the critical buckling mode one (see Fig. 22(b)) as α increases—e.g., note the growing relevance of modes **5** and higher ($\geqslant$**6**), as well as, for large lengths, the evolution of the contributions of modes **3** and **4** towards the combination that characterises the cantilever flexural–torsional critical buckling mode.
(v) Finally, Fig. 24 shows that, generally speaking, the ω_1 load sensitivity increases with the cantilever length (as for the lipped channel beams—see Figs. 13(a) and (b))—indeed, except for α values very close to 1.0, the $L = 15$, 30 and 100 cm curves are associated with progressively larger ω_1 drops.
(vi) However, the fundamental frequency of very short cantilevers (e.g., $L = 3$ cm) exhibits a significant load sensitivity—due to their small lengths, compression highly prevails over bending and, thus, the cantilever behaves like a column, which experiences noticeable frequency drops for low α values.
(vii) The various $\omega_\alpha/\omega_{\alpha=0}$ vs. α curves have clearly non-null derivatives for $\alpha = 0$, which is due to the presence of a significant compressive axial force.

5. Conclusion

This work dealt with the development and illustration of a GBT beam finite element formulation for the local and global vibration analysis of open-section thin-walled members subjected to compression and uniform or non-uniform bending (recall that the latter is always associated with shear forces). First, the GBT

[4]This extremely short (unrealistic) cantilever length was considered in order to capture a specific kind of vibration behaviour.

fundamentals were briefly described, together with the main steps and procedures involved in the formulation and numerical implementation of the aforementioned finite element. Then, the proposed approach was employed to investigate the local and global vibration behaviour of (i) simply supported lipped channel beams under uniform and non-uniform bending (the latter due to uniformly distributed transverse loads) and (ii) plain channel cantilevers acted upon by axial and transverse tip loads—the study focused on the influence of the applied loading level on the vibration frequencies and mode shapes.

It was concluded that the effect of the presence of applied bending moments on the member fundamental vibration frequency increases with length—moreover, even small applied moments can cause noticeable qualitative vibration mode shape changes, a feature not shared by columns. Additionally, it was also found that the moment gradients, and ensuing shear forces/stresses, may lead to natural frequencies much lower than those associated with uniform bending, namely in short beams under high applied loading levels. Finally, the unique modal characteristics of GBT (i) made it possible to perform accurate vibration analyses involving only a fairly low degree of freedom numbers (between 1% and 20% of those required by similarly accurate identical SFEA) and (ii) enabled vibration mode representations through structurally meaningful modal participation diagrams. For validation purposes, some of the GBT-based results were compared with others, either obtained experimentally (cantilevers only) or obtained by SFEA carried out in the codes ANSYS or ABAQUS—an excellent agreement was found in practically all cases.

Acknowledgments

The first author gratefully acknowledges the financial support provided by FCT—Fundação para a Ciência e Tecnologia (Portugal)—through scholarship No. SFRH/BD/18289/2004.

References

[1] B. Budiansky, R.W. Fralich, Effects of panel flexibility on natural vibration frequencies of box beams, NACA Technical Note TN-3070, 1954.
[2] W.B. Fitcher, E.E. Kordes, Investigation of vibration characteristics of circular arc monocoque beams, NACA Report D-59, 1959.
[3] R.G. Thomson, E.T. Kruszewski, Cross-sectional deformations of monocoque beams and their effects on the natural vibration frequencies, NACA Report D-987, 1961.
[4] M.J. Klausbruckner, R.J. Pryputniewicz, Theoretical and experimental study of coupled vibrations on channel beams, *Journal of Sound and Vibration* 183 (1995) 239–252.
[5] S.M. Hashemi, M.J. Richard, Free vibration analysis of axially loaded bending–tension coupled problems: a dynamic finite element, *Computers and Structures* 77 (2000) 711–724.
[6] A. Joshi, S. Suryanarayan, Unified analytical solution for various boundary conditions for the coupled flexural–torsional vibration of beams subjected to axial loads and end moments, *Journal of Sound and Vibration* 129 (1989) 313–326.
[7] A. Joshi, S. Suryanarayan, Iterative method for coupled flexural–torsional vibration of initially stressed beams, *Journal of Sound and Vibration* 146 (1991) 81–92.
[8] C.F. Shih, J.C. Chen, J. Garba, Vibration of a large space beam under gravity effect, *AIAA Journal* 24 (1986) 1213–1216.
[9] M. Ohga, K. Nishimoto, T. Shigematsu, T. Hara, Natural frequencies and mode shapes of thin-walled members under in-plane forces, in: N. Shanmugam, J.Y.R. Liew, V. Thevendran (Eds.), *Thin-Walled Structures—Research and Development*, Elsevier, Amsterdam, 1998, pp. 501–508.
[10] M. Okamura, Y. Fukasawa, Characteristics of instability of local vibration of the thin-walled members under periodic axial forces, *Structural and Earthquake Engineering (JSCE)* 15 (1998) 215s–223s.
[11] O.C. Zienkiewicz, R.L. Taylor, *The Finite Element Method*, fifth ed., Butterworth-Heinemann, Oxford, 2000.
[12] Y.K. Cheung, L.G. Tham, *The Finite Strip Method*, CRC Press, Boca Raton, FL, 1998.
[13] R. Schardt, *Verallgemeinerte Technische Biegetheorie*, Springer, Berlin, Germany, 1989.
[14] D. Camotim, N. Silvestre, R. Bebiano, GBT local and global vibration analysis of thin-walled members, in: N.E. Shanmugam, C.M. Wang (Eds.), *Dynamics of Plated Structures: Analysis and Design*, Woodhead Publishing Ltd., Cambridge, 2007, pp. 36–76.
[15] D. Camotim, N. Silvestre, R. Gonçalves, P.B. Dinis, GBT analysis of thin-walled members: new formulations and applications, in: J. Loughlan (Ed.), *Thin-Walled Structures: Recent Advances and Future Trends in Thin-Walled Structures Technology*, Canopus Publishing, Bath, 2004, pp. 137–168.
[16] D. Camotim, N. Silvestre, P.B. Dinis, Numerical analysis of cold-formed steel members, *International Journal of Steel Structures* 5 (2005) 63–78.
[17] R. Schardt, D. Heinz, Vibrations of thin-walled prismatic structures under simultaneous static load using generalized beam theory, in: W. Krätzig, et al. (Eds.), *Structural Dynamics*, Balkema, Rotterdam, 1991, pp. 921–927.

[18] N. Silvestre, Generalised Beam Theory: New Formulations, Numerical Implementation and Applications, Ph.D. Thesis, DECivil/IST, Technical University of Lisbon, 2005 (in Portuguese).
[19] N. Silvestre, D. Camotim, Generalised beam theory to analyse the vibration behaviour of FRP composite thin-walled members, 2008, submitted for publication.
[20] N. Silvestre, D. Camotim, Vibration behaviour of axially compressed cold-formed steel members, *Steel and Composite Structures* 6 (2006) 221–236.
[21] N. Silvestre, D. Camotim, GBT-based local and global vibration analysis of loaded composite thin-walled members, *International Journal of Structural Stability and Dynamics* 6 (2006) 1–29.
[22] B.Z. Vlasov, *Thin-Walled Elastic Bars*, Fizmatgiz, Moscovo, 1959 (English translation: Israel Program for Scientific Translation, Jerusalem, 1961).
[23] R. Bebiano, N. Silvestre, D. Camotim, GBT formulation to analyze the buckling behavior of thin-walled members subjected to non-uniform bending, *International Journal of Structural Stability and Dynamics* 7 (2007) 23–54.
[24] P.B. Dinis, D. Camotim, N. Silvestre, GBT formulation to analyse the buckling behaviour of thin-walled members with arbitrarily 'branched' open cross-sections, *Thin-Walled Structures* 44 (2006) 20–38.
[25] R.W. Clough, J. Penzien, *Dynamics of Structures*, second ed., McGraw-Hill, New York, 1993.
[26] C. Yu, B.W. Schafer, Effect of longitudinal stress gradients on elastic buckling of thin plates, *Journal of Engineering Mechanics (ASCE)* 133 (2007) 452–463.
[27] Y.K. Cheung, M.S. Cheung, Natural vibrations of thin, flat-walled structures with different boundary conditions, *Journal of Sound and Vibration* 18 (1971) 325–337.